

**INVESTIGATION OF STRUCTURAL  
LUBRICITY ON PLATINUM  
NANOPARTICLES UNDER AMBIENT  
CONDITIONS**

A THESIS SUBMITTED TO  
THE GRADUATE SCHOOL OF ENGINEERING AND SCIENCE  
OF BILKENT UNIVERSITY  
IN PARTIAL FULFILLMENT OF THE REQUIREMENTS FOR  
THE DEGREE OF  
MASTER OF SCIENCE  
IN  
MECHANICAL ENGINEERING

By

Alper Özoğul

May, 2017

INVESTIGATION OF STRUCTURAL LUBRICITY ON PLATINUM  
NANOPARTICLES UNDER AMBIENT CONDITIONS

By Alper Özoğul

May, 2017

We certify that we have read this thesis and that in our opinion it is fully adequate, in scope and in quality, as a thesis for the degree of Master of Science.

---

Mehmet Zeyyad Baykara (Advisor)

---

Mehmet Selim Hanay

---

Hande Toffoli

Approved for the Graduate School of Engineering and Science:

---

Ezhan Karaşan  
Director of the Graduate School

## ABSTRACT

# INVESTIGATION OF STRUCTURAL LUBRICITY ON PLATINUM NANOPARTICLES UNDER AMBIENT CONDITIONS

Alper Özoğul

M.S. in Mechanical Engineering

**Advisor:** Mehmet Zeyyad Baykara

May, 2017

Structural lubricity describes a state of ultra-low friction involving relative motion between atomically flat and molecularly clean surfaces with incommensurate structures. While the occurrence of structural lubricity was quantitatively confirmed under ultrahigh vacuum (UHV) conditions first, recently reported experiments have demonstrated that structurally lubric sliding is achievable under ambient conditions as well, specifically at mesoscopic interfaces formed between thermally deposited gold nanoparticles and graphite.

The question that is covered in this thesis is whether the observation of structural lubricity under ambient conditions is limited solely to gold nanoparticles. To answer this question, an investigation of the frictional behavior of platinum nanoparticles laterally manipulated on graphite has been conducted. In particular, platinum nanoparticles have been prepared by e-beam evaporation of a thin film of platinum on graphite, followed by post-deposition annealing. Morphological characterization of the particles was performed via scanning electron microscopy (SEM) and transmission electron microscopy (TEM), revealing a crystalline structure. X-Ray photoelectron spectroscopy (XPS) revealed no significant change in the electronic structure of platinum upon exposure to air, ruling out the oxidation of platinum nanoparticles under ambient conditions. This finding was supported by cross-sectional TEM measurements demonstrating the absence of an oxide layer on the particle surfaces.

Lateral manipulation experiments have been performed on platinum nanoparticles of mesoscopic dimensions (4000 – 75,000 nm<sup>2</sup>) under ambient conditions via atomic force microscopy (AFM), whereby results indicated the occurrence of structural lubricity, although with a higher magnitude of friction forces when compared with gold nanoparticles. Thus, it is confirmed that the occurrence of structural lubricity between incommensurate, atomically flat surfaces should be independent of material choice, as stated in the theory.

Lastly, an attempt has been made to alter the structure and chemistry of the sliding surface of platinum nanoparticles. For this purpose, platinum nanoparticles have been oxidised in a reactive oxygen plasma atmosphere. XPS results confirmed the existence of oxidised platinum, and structural characterization performed by SEM showed that there was no significant change in morphology. Lateral manipulation experiments performed on oxidised platinum nanoparticles showed that these nanoparticles experience approximately two times as much friction as platinum nanoparticles. The potential reasons behind this observation are discussed.

**Keywords:** Structural Lubricity, Superlubricity, Nanotribology, Nanoparticles, Atomic Force Microscopy, Friction Force Microscopy

## ÖZET

# PLATİN NANOPARÇACIKLARIN ORTAM KOŞULLARINDA YAPISAL KAYGANLIĞININ ARAŞTIRILMASI

Alper Özoğul

Makine Mühendisliği, Yüksek Lisans

**Tez Danışmanı:** Mehmet Zeyyad Baykara

Mayıs, 2017

“Yapısal kayganlık” terimi; atomik derecede düz, moleküler seviyede temiz ve yapısal olarak uyumsuz kristal yüzeylerinin birbirleri üzerinde kayarken sergiledikleri çok düşük sürtünme halini tanımlar. Yapısal kayganlık nicel olarak ilk defa ultra yüksek vakum (UHV) koşullarında gözlemlenmiştir. Yakın zamanda, grafit üzerine ısıl olarak buharlaştırılan altın nanoparçacıklar vasıtasıyla, yapısal kayganlığın ortam koşullarında da elde edilebileceği kanıtlanmıştır.

Bu tezin cevaplamaya çalıştığı soru, yapısal kayganlığın ortam koşullarında sadece altın nano parçacıklara özgü olup olmadığıdır. Bu soruyu cevaplamak için grafit üzerinde yanal olarak manipüle edilen platin nanoparçacıkların sürtünme davranışları incelenmiştir. Bu amaçla, çok düşük miktarda platin, grafit yüzey üzerine elektron demeti ile buharlaştırma tekniği kullanılarak ince film olarak yerleştirilmiş, ardından tavlama işlemine maruz bırakılmıştır. Bu şekilde elde edilen nanoparçacıkların yapısal özellikleri geçirimli elektron mikroskobu (TEM) ve taramalı elektron mikroskobu (SEM) yardımıyla belirlenmiş ve kristal yapıda oldukları onaylanmıştır. X-ışını fotoelektron spektroskopisi (XPS) ölçümleri, havaya maruz kalan platinin elektron spektrumunda yapısal bir değişiklik olmadığını açığa çıkarmış, bu şekilde platin nanoparçacıkların ortam koşullarında oksitlenmediği anlaşılmıştır. Kesit alan geçirimli elektron mikroskobu (X-TEM) ölçümlerinde parçacık yüzeylerinde herhangi bir oksit katmanına rastlanmaması da bu sonucu desteklemektedir.

Mezoskopik boyutlara sahip (4000 – 75.000 nm<sup>2</sup>) platin nanoparçacıklar üzerinde ortam koşulları altında atomik kuvvet mikroskobu (AFM) vasıtasıyla yanal manipülasyon deneyleri gerçekleştirilmiştir. Elde edilen sonuçlar, altın nanoparçacıklarla karşılaştırıldığında daha yüksek sürtünme kuvvetlerine işaret etse de, platin nanoparçacıklar için de ortam koşulları altında yapısal kayganlığın gerçekleştiğini göstermektedir. Böylece, atomik derecede düz ve yapısal olarak uyumsuz kristal yüzeyleri için yapısal kayganlığın, teori tarafından belirtildiği şekilde, malzeme seçiminden bağımsız olarak gerçekleştiği onaylanmıştır.

Son olarak, platin nanoparçacıkların kayan yüzünün yapısını ve kimyasını değiştirmek adına bir deneme yapılmıştır. Bu amaçla, platin nanoparçacıklar reaktif oksijen plazması atmosferine maruz bırakılmıştır. Bu parçacıklarda oksidasyonun varlığı XPS ölçümleriyle kanıtlanmış, SEM görüntüleri vasıtasıyla gerçekleştirilen yapısal karakterizasyonda parçacıkların morfolojisinde kayda değer bir fark görülmemiştir. Oksitlenmiş platin nanoparçacıklar üzerinde gerçekleştirilen yanal manipülasyon deneylerinde, bu parçacıkların platin nanoparçacıklara göre yaklaşık iki kat daha fazla sürtünme kuvveti deneyimledikleri gözlemlenmiştir. Bu gözlemin ardında yatan muhtemel sebepler tartışılmıştır.

**Anahtar Kelimeler:** Yapısal Kayganlık, Süperkayganlık, Nanotriboloji, Nanoparçacıklar, Atomik Kuvvet Mikroskopisi, Sürtünme Kuvvet Mikroskopisi

# Acknowledgement

Firstly, and mostly, I would like to thank Prof. Mehmet Baykara for his endless support and encouragement throughout this work. In the five years I worked with him, I have witnessed his enthusiasm and passion for research, and I could boldly say that a portion of these have passed on to me. He, both as an academic advisor and as a person, is one of the most influential people I have ever met, if not the most influential.

Also, technical personnel in UNAM, especially Mustafa Güler, deserve a special mention for the countless work hours they spent on keeping the equipment in perfect working condition for the experimental steps of this thesis. Without them, this work would be impossible.

I also thank the members of the Scanning Probe Microscopy research group, namely Tarek Abdelwahab, Arda Balkancı, Ebru Cihan, Tuna Demirbaş, Verda Saygın, Zeynep Melis Süar and Berkin Uluutku, for their company as friends and as colleagues; and I wish them the best in their academic journey.

I would like to thank all my friends in Bilkent, especially in the Mechanical Engineering department, for their support and the times we have spent together. Priceless memories I have with them will be remembered for my whole life.

Finally, I would like to thank my family for their endless belief in me, and their support during my whole life. Their love and care has made me the person I am, and I cannot be grateful enough for the countless times that I have hit a wall in my personal or academic life, where they would be ready to get me back on the track.

*To My Parents and My Future Family*

# Contents

<b>Acknowledgement .....</b>	<b>vii</b>
<b>List of Figures.....</b>	<b>xi</b>
<b>List of Tables .....</b>	<b>xv</b>
<b>1. Introduction.....</b>	<b>1</b>
1.1 Friction: A Brief Survey.....	1
1.2 Nanotribology: Atomic Roots of Friction.....	2
1.3 Structural Lubricity .....	5
1.4 Outline.....	8
<b>2. Experimental Methods .....</b>	<b>9</b>
2.1 Scanning Electron Microscopy .....	9
2.2 Transmission Electron Microscopy .....	12
2.3 X-Ray Photoelectron Spectroscopy .....	16
2.4 Atomic Force Microscopy.....	18
2.4.1 Friction Force Microscopy.....	23
2.4.2 Cantilever Calibration .....	25
<b>3. Sample Preparation and Characterization.....</b>	<b>28</b>
3.1 Sample Preparation .....	28
3.1.1 Preparation of Platinum Nanoparticles .....	28

3.1.2	Preparation of Oxidised Platinum Nanoparticles .....	32
3.2	Sample Characterization .....	33
3.2.1	Structural Characterization via SEM and TEM .....	33
3.2.2	Chemical Characterization via XPS.....	37
<b>4.</b>	<b>Nanomanipulation Experiments on Platinum Nanoparticles .....</b>	<b>43</b>
4.1	Manipulation Experiments on Platinum Nanoparticles: Confirmation of Structural Lubricity .....	43
4.2	Manipulation Experiments on Oxidised Platinum Nanoparticles .....	48
<b>5.</b>	<b>Summary and Outlook .....</b>	<b>52</b>
	<b>Bibliography .....</b>	<b>54</b>

# List of Figures

<b>Figure 1.1</b> Picture of the first scanning tunnelling microscope developed by Gerd Binnig and Heinrich Rohrer at IBM Research Laboratory in Zurich. Image by J Brew, licensed under CC BY-SA 2.0. ....	4
<b>Figure 1.2</b> The structural lubricity phenomenon occurs when two crystalline, atomically flat surfaces with incommensurate structures slide on each other. As the number of atoms increase, the potential energy barrier that each atom needs to surmount decreases, resulting in a sub-linear relationship between total friction force and number of sliding atoms. Adapted from [29]. ....	7
<b>Figure 2.1</b> Schematic of a scanning electron microscope. Taken from [34]. ....	10
<b>Figure 2.2</b> Regions where signals are originated in scanning electron microscopy. Backscattered electrons also originate from the region where the secondary electrons emerge from, and characteristic X-rays originate from the entire excited volume. ....	11
<b>Figure 2.3</b> FEI Quanta 200 FEG SEM used for the experiments presented in this thesis. ....	12
<b>Figure 2.4</b> Selected area diffraction patterns for single crystal (left), polycrystalline (middle) and amorphous (right) specimens. Taken from [35]. ....	14
<b>Figure 2.5</b> HAADF image of an oxidised platinum nanoparticle. ....	14
<b>Figure 2.6</b> FEI Tecnai G2 F30 TEM used for the experiments presented in this thesis. ....	15
<b>Figure 2.7</b> Example XPS survey spectrum taken on platinum nanoparticles deposited on graphite. ....	17

<b>Figure 2.8</b> Thermo Scientific K-Alpha XPS used for the experiments in this thesis..	17
<b>Figure 2.9</b> Schematic of the AFM setup, and the sketch of the AFM tip, which is considered as a single asperity contact. Adapted from [36].....	20
<b>Figure 2.10</b> Contact mode AFM image of platinum nanoparticles deposited on graphite.....	21
<b>Figure 2.11</b> PSIA XE-100E AFM used for the experiments presented in this work. .	23
<b>Figure 2.12</b> Schematics of several model sample surfaces are shown on the left and recorded lateral force signals on the right. Surface regions with darker colors correspond to higher coefficients of friction. As one can easily see, a change in height (but not in friction coefficient) would cause the cantilever to torsionally twist in the same manner as it would upon a change in friction coefficient, and result in an artificial “friction signal”. Adapted from [37]. .....	24
<b>Figure 2.13</b> Schematic of a friction loop, where the friction loop half-width is denoted by the green arrow and the offset from zero is denoted with the full, light blue line. Dashed blue lines show mean signals in the forward and backward scanning directions. ....	25
<b>Figure 2.14</b> Schematic drawing of the MikroMasch TGF11 lateral force grating used for lateral calibration. (100) and (111) refer to the crystallographic planes of Si. Taken from [42]. ....	27
<b>Figure 3.1</b> Vaksis MIDAS E-Beam evaporation system used for sample preparation. ....	29
<b>Figure 3.2</b> Large-scale SEM micrograph of platinum deposited on a clean HOPG surface via e-beam evaporation.....	30
<b>Figure 3.3</b> Rapid thermal annealing (RTA) system used to prepare samples. ....	31
<b>Figure 3.4</b> Large-scale SEM micrograph of the HOPG surface decorated with platinum nanoparticles after post-deposition annealing.....	31
<b>Figure 3.5</b> SEM micrographs of over-exposed platinum nanoparticles (left) and platinum nanoparticles oxidised with optimal parameters (right).....	32
<b>Figure 3.6</b> Bright field TEM (left) and HRTEM (right) micrographs of platinum nanoparticles. ....	34
<b>Figure 3.7</b> Selected area diffraction pattern gathered from platinum nanoparticles. ..	34

<b>Figure 3.8</b> FEI Nova 600i Nanolab FIB device used to prepare cross-sectional TEM samples.....	35
<b>Figure 3.9</b> Cross-sectional TEM micrographs taken from the bottom (sliding) surface (left) and the top surface (right) of a platinum nanoparticle. Top side of the left image is platinum, and the bottom side is graphite. Top side of the right image is epoxy, and the bottom side is platinum. Atomic planes of platinum proceeding all the way to the top and bottom surfaces, as well as the absence of an amorphous oxide layer, are clearly observed. ....	36
<b>Figure 3.10</b> Cross-sectional TEM micrographs taken from the bottom (sliding) surface (left) and the top surface (right) of an oxidised platinum nanoparticle. Top side of the left image is graphite, and the bottom side is nanoparticle. Top side of the right image is nanoparticle, and the bottom side is epoxy. The hexagonal patterns are caused by the tilted angle of the sample with respect to the incident electron beam...	37
<b>Figure 3.11</b> XPS spectra taken in specified energy ranges from Pt nanoparticles deposited on HOPG. Top left: O range (525-545 eV); top middle: C1s range (278-297 eV); top right: Pt4f range (64-87 eV); bottom: wide survey.....	38
<b>Figure 3.12</b> XPS spectra taken from oxidised platinum nanoparticles deposited on HOPG. Top left: O range (525-545 eV); top middle: C1s range (278-297 eV); top right: Pt4f range (64-87 eV); bottom: wide survey.....	39
<b>Figure 3.13</b> Peak-fitted XPS data taken from oxidised platinum nanoparticles deposited on HOPG. ....	41
<b>Figure 3.14</b> Cross-sectional HAADF image (left) and EDX line profile taken for oxygen (right) of an oxidised platinum nanoparticle. The nanoparticle is oriented such that the left side of the image is graphite and the right side is epoxy. ....	42
<b>Figure 3.15</b> Cross-sectional HAADF image of an oxidised platinum nanoparticle (left) and EDX map for oxygen performed on the same area (right). In the EDX map, brightness indicates oxygen content, and the nanoparticle is oriented in the same way as it is in Figure 3.14. ....	42
<b>Figure 4.1</b> A schematic of manipulation experiments. For small normal forces, the tip may climb on top of the particle and thus, “image” it (top). If the normal force is above a threshold value, the tip pushes the particle from the side, thus manipulating it (bottom).....	44

**Figure 4.2** AFM images detailing the manipulation of a platinum nanoparticle. Left: Topography image of the manipulated nanoparticle; Middle: Topography image of the nanoparticle after manipulation; Right: Lateral force image taken during manipulation. .... 45

**Figure 4.3** Friction force versus contact area data points gathered from nanomanipulation experiments performed on platinum and gold nanoparticles. .... 46

**Figure 4.4** Normalized friction versus number of sliding atoms for platinum nanoparticles. The blue dashed line and the red solid line denote the upper and lower theoretical limits of the scaling factor  $\gamma$  for structural lubricity, respectively. The cyan dashed line shows the average  $\gamma$  for all investigated nanoparticles. .... 47

**Figure 4.5** Friction versus contact area data points gathered from oxidised platinum nanoparticles sliding on graphite (red), compared with gold (blue) and platinum (black) data points. The plot has been divided into two size regimes, where regime 2 includes data points relevant for a comparison of friction forces between the different types of materials ..... 50

**Figure 4.6** RMS roughness histograms of HOPG in non-oxidised (left) and oxidised (right) samples..... 51

## List of Tables

<b>Table 3.1</b> Comparison of experimental spectrum peak positions of Figure 3.13 and reference peak positions.....	41
<b>Table 4.1</b> Mean friction forces and standard deviations for gold, platinum and oxidised platinum nanoparticles with similar contact areas.....	50

# Chapter 1

## Introduction

### 1.1 Friction: A Brief Survey

Friction is a ubiquitous phenomenon that affects our daily lives drastically. Even the most basic actions such as walking or holding objects [1] are dominated by friction. Furthermore, friction constitutes an important portion of tactile sensing [2]. However, like many other physical phenomena, friction also has negative effects. For instance, friction is considered as the main mechanism responsible for energy dissipation [3]. It is reported that one third of the fuel energy produced in a car [4], 32% of energy needed to produce paper [5], and 26% of the fuel energy produced in heavy duty road vehicles (i.e. trucks, trailers, buses and coaches) [6] is lost due to friction. From these examples it can be easily inferred that understanding friction is critical both for technological applications and explaining related physical phenomena.

Because of its very common occurrence in nature, friction was one of the earliest natural phenomena discovered and utilized by humans, from the Lower Palaeolithic Era (~1 million years ago) where the friction between two sticks was used to create fire [7], to Ancient Egypt where the earliest use of lubrication is recorded [8]. The first

scientific approach to friction dates back to 1493 by Leonardo da Vinci. He conducted experiments on lubricated contacts which led to the laws of sliding friction; however these results were not published during his lifetime [9]. First recorded works on the laws of friction were published approximately 200 years later by Guillaume Amontons. Amontons reported two out of three laws of friction, which are:

- The force of friction is directly proportional to the applied load.
- The force of friction is independent of the apparent area of contact [10].

Amontons' two discoveries led to the widely known formula for friction:

$$F_f = \mu F_n \quad (1.1)$$

Here,  $F_f$  is friction force,  $F_n$  is the normal force acting between the surfaces in contact, and  $\mu$  is called the coefficient of friction. The third law of friction was discovered by Charles-Augustin de Coulomb, which is:

- Kinetic friction is independent of the sliding velocity.

These discoveries, however, failed to give a complete understanding of what friction really is, what the coefficient of friction depends on and why non-linear effects are often observed [11]. While many researchers over centuries tried to solve the “mystery” of friction, a complete understanding on this subject is not yet achieved. This is due to the complex nature of friction, which is affected by the adhesion force between surfaces, surface roughness, and elasticity of the sliding surfaces, among others [12]. The field of *tribology*, namely the study of friction, lubrication and wear, however, has gained significant momentum during the last few decades, due to advances in experimental techniques. In particular, studies of *nanotribology* (the investigation of friction, lubrication and wear on the nanometre scale (0-100 nm)) have made breakthroughs in the field [13] [14].

## 1.2 Nanotribology: Atomic Roots of Friction

Experimental work on nanotribology was made possible thanks to the development of devices such as the surface force apparatus (SFA) and the atomic force microscope

(AFM), allowing friction measurements on surfaces with very high resolution in both force (down to pN range) and position (down to several Å). The SFA technique was invented by Tabor and Winterton in 1969, where it was first used to measure van der Waals forces between smooth mica surfaces [15]. In this technique, two cylinders with axes perpendicular to each other are approached in a very precise fashion, and the forces exerted on the surfaces are measured while the surfaces move with respect to each other. The AFM was developed shortly after the Nobel-Prize-winning invention of the scanning tunnelling microscope (STM) by Binnig and Rohrer in 1981 (Figure 1.1) [16]. The main working principle of STM is the tunnelling effect, which involves flow of electrons between two conductive surfaces with a voltage difference that are sufficiently close to each other. In STM, a substrate surface and a thin wire (STM tip), commonly made of tungsten or platinum - iridium, are the conductors between which electron tunnelling occurs. By fixing the tunnelling current via controlling the tip – sample distance during scanning at a constant voltage, the STM tip can produce topographic maps of various surfaces on the sub-nanometre scale. The AFM technique, invented by Binnig, Quate and Gerber in 1986 [17], is quite similar to STM since they both belong to the family of scanning probe microscopy (SPM) devices; however, the working principles are different. At the heart of the AFM there is a micro-machined flexible cantilever with a sharp tip protruding towards the sample direction. Here, physical interactions between the tip and sample, e.g. van der Waals or electrostatic forces, cause the cantilever beam to deflect, and this deflection is measured by the displacement of a laser beam reflected from the top side of cantilever onto a position-sensitive photodetector. This technique, which allows very high-resolution topographical mapping as well as precise measurement of forces on surfaces, will be discussed further in Section 2.4.

The importance of nanotribology arises from the fact that on the macroscale, the *apparent* contact area (which, in most cases, appears *smooth* to the naked eye) is different from the *true* contact area, which consists of *multiple asperities* with dimensions that have a range from several micrometres to a few atoms. This severely complicates the physical interpretation of friction experiments performed on the macroscale. The possibility of having a *single asperity contact*, provided by AFM thanks to the availability of an extremely sharp tip, creates a whole new perspective to

understand friction on a fundamental level. The main technique with which single-asperity-contact friction experiments are performed is *friction force microscopy* (FFM). FFM is simply a variation of AFM, and a typical AFM setup is used in this technique. Unlike AFM, where only the bending deflection of the cantilever caused by surface forces applied to the AFM tip in the normal direction is detected; in FFM, both the bending deflection and the torsional twisting, which is caused by the forces acting on the AFM tip in the lateral direction, are measured. By detecting the torsional twisting of the cantilever, the friction force experienced by the AFM tip can be determined in a precise fashion. Some of the most important results in nanotribology have been obtained by using this technique, e.g. the stick-slip behavior of atomic scale friction [18] and *superlubric* sliding among graphite flakes [19] [20] .

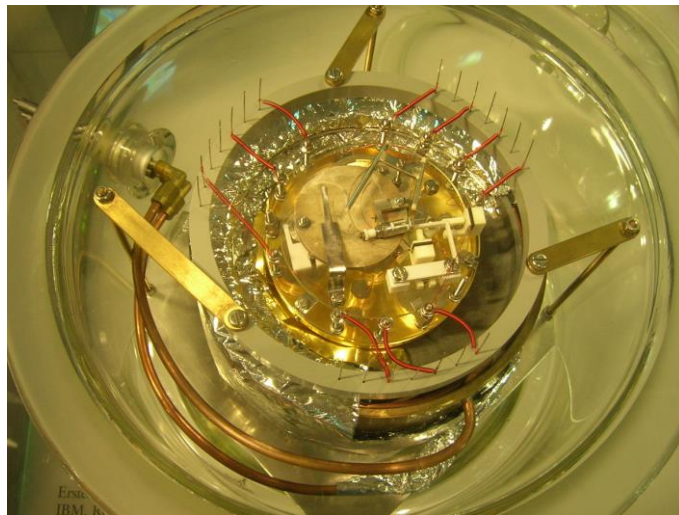


**Figure 1.1** Picture of the first scanning tunnelling microscope developed by Gerd Binnig and Heinrich Rohrer at IBM Research Laboratory in Zurich. Image by J Brew, licensed under CC BY-SA 2.0.

Like any experimental method, however, FFM has certain limitations. To name a few:

- In FFM experiments, the contact area is limited by the size of the AFM tip. Although there is the possibility to increase the area by coating the tip with certain materials like gold, this also makes the tip blunter, resulting in a decrease in spatial resolution. It is known that the contact area of the slider has a significant effect on the friction [13], so the ability to control this variable without affecting the FFM setup is critical.

- Since conventional AFM cantilevers are manufactured from a small set of materials; i.e. silicon, silicon dioxide, silicon nitride, there is a limited number of material combinations that can be used in FFM experiments.
- Due to resolution-related limitations of imaging techniques, structural and chemical characterization of the AFM tip apex on the atomic scale is an important challenge. As it is known that both the interface structure and the chemical composition of the surfaces forming the interface have significant contributions to friction on the nanoscale, this limitation constitutes an important problem.

To overcome these limitations, a method that involves nanoparticle sliders manipulated by an AFM tip has been proposed [21] [22]. In this method, instead of using the AFM tip directly as the slider, nanoparticles composed of an arbitrary material are used. These nanoparticles are manipulated by pushing them laterally with the AFM tip, and the torsional twisting of the tip during the manipulation due to the friction force experienced by the particle, is measured. Previously, this technique was used by our research group to demonstrate the *structurally lubric* (which will be discussed in the next section) sliding behaviour of gold nanoparticles on a graphite surface under ambient conditions [23]. Since nanoparticles can be prepared with a good degree of control regarding desired shapes and sizes, and from a wide selection of materials, most of the main limitations of the FFM technique listed above can be overcome using this experimental method.

### 1.3 Structural Lubricity

On the atomic scale, friction is caused by the *atomistic locking* of the slider's atoms on those of the substrate; which means that the slider atoms, as they are moving along the potential energy landscape of the substrate, will be trapped in the potential energy minima of the substrate lattice. To enable relative motion between the surfaces, these energy barriers need to be surmounted by the slider atoms. To complicate the situation further, the slider might deform elastically to fit into the substrate surface, increasing

the number of atoms locked in the substrate potential energy landscape. Moreover, contaminant molecules in the surroundings can create an intermediate layer between the sliding surfaces; since these mobile molecules would get trapped in the potential energy minima of both the slider and the substrate, this would cause additional locking between the two surfaces. Theoretical studies of atomic-scale friction have shown that when an atomically flat, crystalline slider moves on a substrate which is also atomically flat and crystalline, in the absence of contaminant molecules (corresponding to an ultrahigh vacuum (UHV) environment) and when the slider and the substrate surfaces are *incommensurate* (meaning that due to the difference of the lattice constants, slider atoms would not perfectly fit into the potential energy minima of the substrate), a state of very low friction frequently referred to as *superlubricity* would be observed [24] [25]. This phenomenon was, for instance, experimentally studied and confirmed between individual graphite flakes with different angular differences between the respective crystal lattices [19] [20]. The name superlubricity, however, is debated, since it gives the impression that friction disappears completely, in analogy to superconductivity. It is therefore proposed to use the term *structural lubricity* instead, which would definitively indicate that the state of very low friction is occurring solely due to the incommensurate structures of the sliding surfaces [24], although superlubricity is still used commonly [26] [27] [28].

To further explain this phenomenon, the smallest possible slider, which is a single atom, moving along the potential energy landscape of an atomically-flat, crystalline substrate can be considered (Figure 1.2). Along its motion, the sliding atom will be trapped in potential energy minima of  $\Delta E$ , which can be characterized by the interaction between the slider and the substrate as the diffusion energy barrier of the slider atom on the substrate. When the size of the slider increases from one atom to two and more atoms, the lattice mismatch between the crystalline slider and the substrate will lower the potential energy minimum needed to maintain motion per atom, which would result in a sub-linear relation between the total friction force and the number of sliding atoms. This relation is characterized as:

$$F_f = F_0 N^\gamma \quad (1.2)$$

where  $F_0$  is the friction force experienced by a one-atom-slider on the substrate, defined as the ratio of diffusion energy barrier  $\Delta E$  to the lattice constant of the substrate  $a$ ;  $N$  is the number of atoms on the sliding surface, and  $\gamma$  is the scaling factor, which takes values between 0 and 0.5 [21]. The theoretical limits of the scaling factor are determined by considering rigid, crystalline slider-substrate pairs where the relative angular orientation is variable [29].

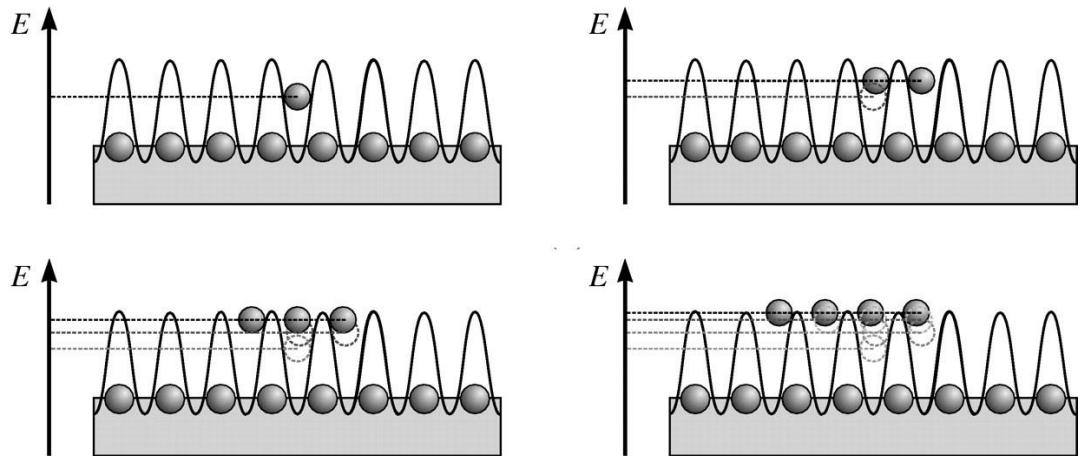


**Figure 1.2** The structural lubricity phenomenon occurs when two crystalline, atomically flat surfaces with incommensurate structures slide on each other. As the number of atoms increase, the potential energy barrier that each atom needs to surmount decreases, resulting in a sub-linear relationship between total friction force and number of sliding atoms. Adapted from [30].

Structural lubricity has been previously observed and quantitatively confirmed between gold nanoparticle sliders and a graphite substrate [21]. These experiments were conducted under UHV conditions in order to drastically reduce the number of contaminant molecules in the environment. Previously, it was thought that structural lubricity can only be observed under UHV conditions [31]; however, it was recently shown that gold nanoparticle sliders manipulated on a graphite substrate also slide in structurally lubric fashion under ambient conditions [23]. Specifically, it was demonstrated via DFT (*density functional theory*) calculations that the distance between the sliding surfaces is too small for common contaminant molecules such as water and oxygen to breach, which essentially leads to the existence of an atomic-scale “hermetic seal” around the interface and the conservation of structural

lubricity [23]. The question that is investigated in this thesis is inspired from this work, namely whether structural lubricity under ambient conditions can only be observed for the specific slider-substrate combination of gold and graphite, or whether it can be extended to other noble metals such as platinum.

## **1.4 Outline**

The rest of this thesis consists of four chapters:

In Chapter 2, experimental methods used in this work are introduced. These methods can be grouped into two sections: sample characterization and nanomanipulation. Sample characterization methods consist of scanning electron microscopy (SEM), transmission electron microscopy (TEM) and X-ray photoelectron spectroscopy (XPS), while nanomanipulation involves atomic force microscopy (AFM). In each section of Chapter 2, the working principle of the respective technique is explained along with the way this technique is used in this work.

In Chapter 3, sample preparation and characterization processes are explained in detail. The first section deals with the preparation of platinum and platinum oxide nanoparticles by e-beam evaporation, post-deposition annealing and plasma oxidation for platinum oxide nanoparticles. The second section deals with sample characterization, which consists of structural characterization by SEM and TEM, and chemical characterization by XPS.

In Chapter 4, nanomanipulation experiments performed on the nanoparticles are discussed along with the results. This chapter is divided into two sections, where in the first section experiments conducted on platinum nanoparticles are explained along with the investigation of structural lubricity, and in the second section experiments performed on platinum oxide nanoparticles are reported.

Lastly, in Chapter 5, a brief summary of the thesis is presented with potential future work that could be done to supplement the results of this study.

# Chapter 2

## Experimental Methods

### 2.1 Scanning Electron Microscopy

Electron microscopy is a microscopy technique that makes use of electrons instead of visible light for imaging. This allows to overcome the diffraction limit of conventional optical microscopes, since electrons' wavelength can be shorter than visible light by a few orders of magnitude. The first electron microscope was developed by Ernst Ruska in 1931 [32], for which he was awarded Nobel Prize in Physics in 1986, along with Gerd Binnig and Heinrich Rohrer, the developers of STM and AFM [33]. This electron microscope was a transmission electron microscope (TEM), which will be discussed in the next section. Scanning electron microscope is a type of electron microscope that utilizes scanning coils to direct the incident electron beam on the sample in the manner of raster scanning. It was first implemented by adding scanning coils to a conventional TEM by von Ardenne [34]. However, modern SEM devices detect backscattered electrons and secondary electrons instead of electrons transmitted through the sample, as in the case of TEM. In SEM, an electron beam, typically in the range of 5-20 keV, is generated from an electron gun, e.g. a tungsten filament, and

then via electromagnetic lenses electrons are accelerated and focused onto a point on the sample. A diagram of the SEM setup can be seen in Figure 2.1. Scanning coils act as a mirror would act on a beam of light, and deflect the electron beam onto the sample. Angles of these scan coils are controlled in a manner to scan the sample point by point. Here, the electron optical components are sealed in vacuum to maximise the mean-free path of the electrons, and the sample is generally placed in a vacuum chamber as well. Electrons incident on the sample interact with the surface atoms, and these interactions result in several events, each containing different information about the sample.

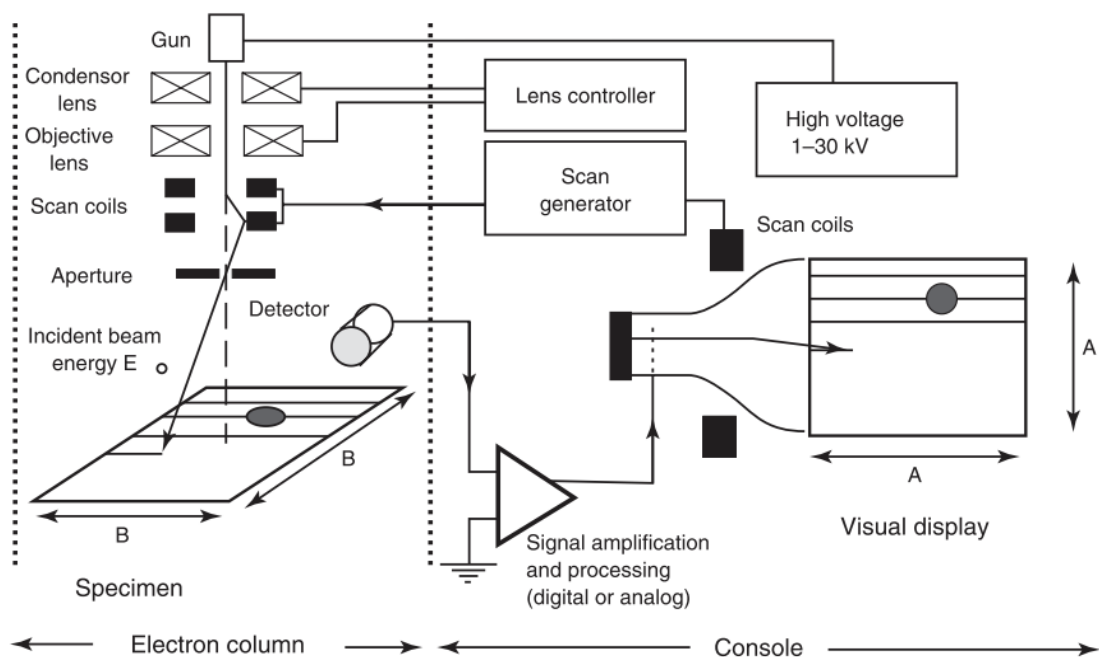


**Figure 2.1** Schematic of a scanning electron microscope. Taken from [35].

In the case of elastic collision between the incident electrons and the sample atoms, electrons are reflected from the surface. These electrons are called *backscattered* electrons since the beam is scattered from the surface. Backscattered electron yield, which is the number of electrons scattered back, is a function of atomic number, since it is a characteristic of the atomic weight. As expected from elastic collisions, electrons colliding with a particle with more mass will have more energy, hence they would be easier to detect. For this case, backscattered electrons are used for atomic number contrast imaging. Additionally, during SEM imaging, sample atoms emit low energy *secondary electrons* as a result of inelastic scattering with beam electrons.

Because of their low energy, secondary electrons can only travel distances in the range of a few nanometers in the sample. For this reason, secondary electrons contain the surface topography information and secondary electron detection is the most common method used in SEM. Another event that could happen during SEM imaging is X-ray irradiation, where the incident electron releases an electron from the sample, whose space will be filled by the electron in the higher energy state. Energy difference between the levels is emitted by means of X-rays, and these X-rays are characteristic to the element. These characteristic X-rays are used in *energy dispersive X-ray spectroscopy* (EDX) to perform elemental analysis of the sample. Finally, electrons can pass through the sample, which is called a *transmission event*, but these electrons are used in TEM, not in SEM.

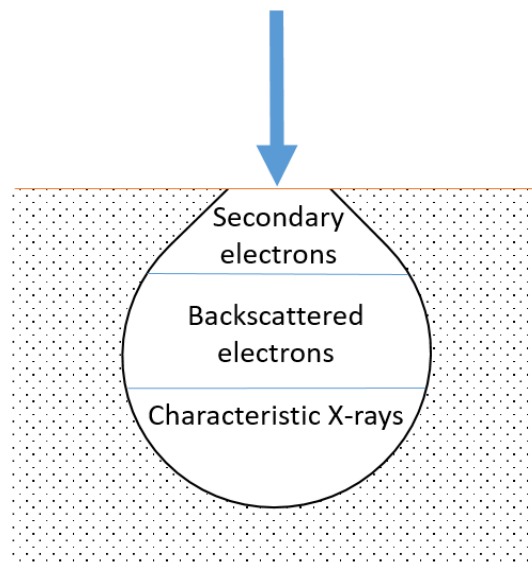


**Figure 2.2** Regions where signals are originated in scanning electron microscopy. Backscattered electrons also originate from the region where the secondary electrons emerge from, and characteristic X-rays originate from the entire excited volume.

In SEM, controllable parameters are electron beam energy, given in units of Volts, spot size, and optical parameters. Electron beam energy determines the depth through which the electron beam penetrates into the sample, and as the beam energy increases electrons will travel further into the sample. Spot size is the diameter of the electron beam incident on the surface, and this parameter is adjusted in order to correct aberrations in set voltage values. Optical parameters, e.g. brightness, contrast and focus, are adjusted to maximise the image quality.



**Figure 2.3** FEI Quanta 200 FEG SEM used for the experiments presented in this thesis.

## **2.2 Transmission Electron Microscopy**

Transmission Electron Microscopy (TEM) is the earliest electron microscopy technique. In TEM, an electron beam is generated in the same manner as SEM, but with relatively higher energy, typically in the range of hundreds of keV. As in SEM, the electron beam is generated from an electron gun, and by means of electron optics, the beam is focused onto the sample. The main difference between SEM and TEM is that in TEM, transmitted electrons are used for imaging. Additionally, in the case of

TEM, electrons can be *diffracted* as they are passing through the sample, and this signal is used for selected area diffraction and high-resolution TEM modes. To make use of transmitted electrons, electron beams initially hit the sample, and then transmitted electrons are converted into an image by means of electron optics. TEM has many operation modes, and several of them are used in the context of this thesis for characterization purposes. In *bright-field TEM*, the objective aperture is placed in a way that only the transmitted electrons and not the diffracted electrons pass through. Since electrons will lose energy depending on the distance they travel inside the specimen, bright-field TEM gives information about the structure of the sample up to a certain resolution limited by the electron optics. This method is analogous to bright-field optical microscopy, where a beam of light incident on the sample is used to generate an image. Orientation of the sample and selection of the area to image is adjusted by the goniometer where the TEM sample is inserted.

Another TEM mode is the *selected area diffraction (SAD)* mode, where the objective aperture is removed, and an intermediate aperture is placed on the image plane in a way that only the diffracted electrons pass through. This signal also includes the incident beam, which has significantly higher energy than the diffracted beam, and in order to prevent damage to the detector, an object, e.g. a pin, is placed in front of the beam, as seen in Figure 2.4. Electrons are diffracted as stated in Bragg's Law,

$$2d\sin\theta = n\lambda \quad (2.1)$$

which correlates the scattering event to the inter-planar spacing of the crystal sample ( $d$ ). The structure of the sample can be deduced from SAD, since an SAD pattern will indicate the positions of the atoms on the imaging plane. In the case of single crystals, spots with positions characteristic to the crystal structure will appear. In the case of polycrystalline materials, continuous rings will appear, and in the case of amorphous materials a continuous radial distribution will appear in the diffraction pattern. From the diffraction pattern, crystal structure and the lattice constant of the material can be obtained (Figure 2.4).

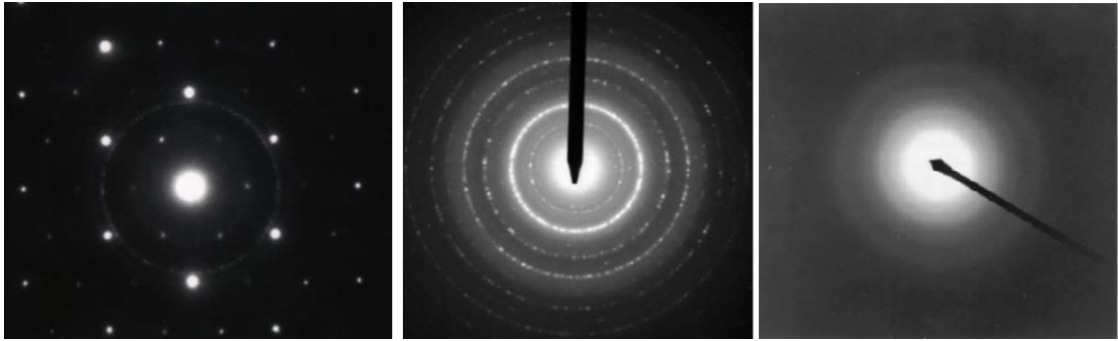


**Figure 2.4** Selected area diffraction patterns for single crystal (left), polycrystalline (middle) and amorphous (right) specimens. Taken from [36].

Another TEM imaging mode is *high-angle annular dark-field* (HAADF) mode. This mode utilizes the scanning TEM (STEM) technique, which is analogous to SEM. In HAADF, incoherent elastically-scattered electrons are used to generate the image (see, e.g. Figure 2.5). These electrons have a high scattering angle, and to detect these, an annulus shaped detector is positioned accordingly. This technique is a dark-field technique since the incident beam does not contribute to the final image, which will increase the contrast of the detected electrons. The intensity of the incoherently scattered beams, as in the backscattered electrons, is a function of the atomic number of the sample. As such, this technique can be used simultaneously with EDX to perform elemental mapping.

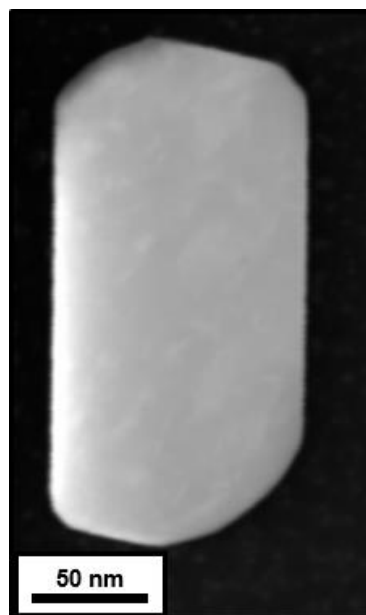


**Figure 2.5** HAADF image of an oxidised platinum nanoparticle.

The final TEM mode to be discussed here is the high-resolution TEM (HRTEM) mode. Somewhat counter-intuitively, HRTEM is not the name given to high-resolution bright field or HAADF images, but a separate technique by itself. To overcome certain limitations of TEM instrumentation and electron optics, images are formed indirectly in this technique. In HRTEM, the interference of transmitted electrons with diffracted electrons is taken as the signal. This signal, where the phase difference of diffracted beams is obtained by taking the transmitted beams as reference, is the Fourier transform of the scattering pattern, which contains information about the atomic orientation. By using this technique, atomic planes of a crystalline sample can be observed directly, and the inter-planar distance can be measured with high precision.



**Figure 2.6** FEI Tecnai G2 F30 TEM used for the experiments presented in this thesis.

## 2.3 X-Ray Photoelectron Spectroscopy

Photoelectron spectroscopy is a spectroscopy technique where the sample is probed by photons to emit electrons. By detecting the energy levels of the emitted electrons, the electronic structure of the sample can be investigated. X-ray photoelectron spectroscopy (XPS) utilizes monochromatic X-rays generated by exciting a magnesium or aluminium source which emits X-Rays via  $K\alpha$  radiation (where an X-ray is generated by ejecting an electron from the  $n=1$  orbital (K), and the closest higher energy electron ( $\alpha$ ) fills the hole while radiating an X-ray to release extra energy). This X-ray beam then strikes the sample and causes core energy level electrons to be released from atoms in the vicinity of the surface. Since the discrete energy levels of the electrons are characteristic to the atomic or molecular orbitals they belong to, by measuring the intensity of the released electrons in a given energy interval via an electron detector, electronic properties of the sample, e.g. the element type and the molecular composition, can be obtained. An example XPS spectrum obtained on platinum nanoparticles deposited on graphite can be seen in Figure 2.7. In this example, there is a large peak at 284.5 eV, which corresponds to the energy of the carbon 1s orbital. Another visible peak is at 75 eV, which corresponds to the energy level of the platinum 4f orbital. Energy levels associated with molecular and atomic orbitals are taken from reference handbooks, where the positions and the shapes of peaks in the XPS spectra of atoms and molecules are reported with references to previous experimental data and calculations; and through standardized curve fitting processes the chemical identity of the sample can be determined. One aspect to consider here is that the peak positions are expected to differ from instrument to instrument by a constant amount. Therefore, to compare spectra taken from different XPS instruments, the well-known and stable carbon 1s energy level is taken as standard, and other energy levels are shifted according to the difference between carbon 1s peak positions in different instruments.

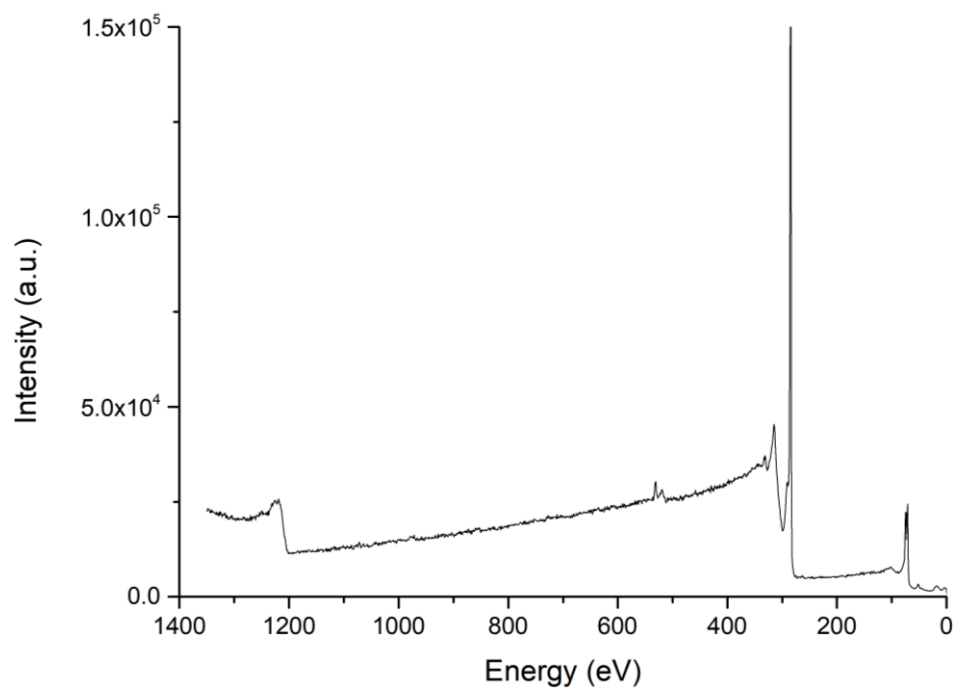


**Figure 2.7** Example XPS survey spectrum taken on platinum nanoparticles deposited on graphite.

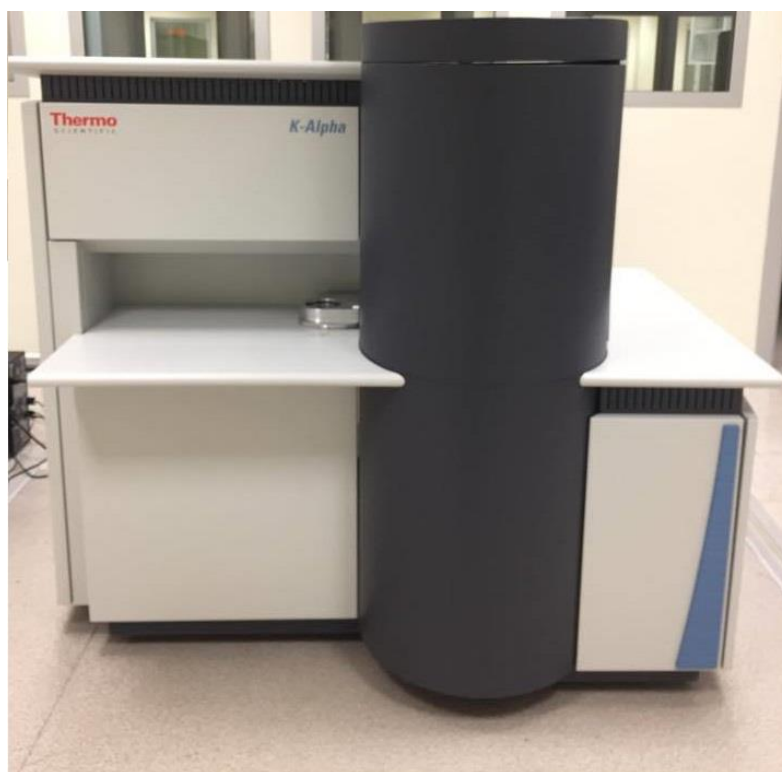


**Figure 2.8** Thermo Scientific K-Alpha XPS used for the experiments in this thesis.

## 2.4 Atomic Force Microscopy

Atomic Force Microscopy (AFM), as mentioned in Chapter 1, is a member of the scanning probe microscopy family, which, at its core, utilizes a cantilevered beam with a sharp tip protruding in the direction of the surface to be imaged (Figure 2.9). As in SEM, the raster scanning method is used to obtain a 2D image, but in AFM the sample is not stationary in most cases. To achieve raster scanning, the sample is moved precisely in two lateral directions, namely the fast-scan and slow-scan directions, by means of piezoelectric actuators. The basic AFM setup consists of these main elements:

- The AFM cantilever, which is the most critical part of AFM. AFM cantilevers are manufactured via micromachining, mainly from Si, SiO<sub>2</sub> and Si<sub>3</sub>N<sub>4</sub>. The “top side” of the cantilever, which is the side opposite to where the AFM tip is located, is coated with a reflective material, generally aluminium or gold. This allows for the laser beam to reflect from the cantilever to the photodetector, which is used to detect the deflection and twisting of the cantilever. Typical AFM cantilevers have stiffness values, denoted  $k$ , ranging from 0.01 N/m to 50 N/m in magnitude. In atomic-resolution, UHV AFM setups, stiff tuning forks (around 2000 N/m) can also be used instead of AFM cantilevers. Dimensions of the AFM cantilevers have a wide range depending on the application, but typically the cantilever length is in the range of hundreds of  $\mu\text{m}$ , the width is in the range of tens of  $\mu\text{m}$  and the thickness is in the range of a few  $\mu\text{m}$ . The most common shape for the AFM tip is a pyramid slanting to the end of the cantilever, but there are AFM tips shaped for specific applications, such as FIB (focused ion beam)-milled high aspect ratio tips. In this work, PPP-XYCONTR AFM cantilevers by Nanosensors™ are used, with 450  $\mu\text{m}$  length, 50  $\mu\text{m}$  width and 2  $\mu\text{m}$  thickness.
- To detect the deflection of the cantilever, the most common method used is the beam deflection method. In this method, a laser beam created by a laser diode is reflected off the cantilever’s reflective top surface to a position-sensitive photodetector (PSPD) arranged into four quadrants of a

square. At the beginning of an experiment, the position of the laser and the PSPD is adjusted such that the reflected laser beam is in the centre of the PSPD square. Bending and torsion of the cantilever causes the laser beam spot to move either vertically or horizontally on the PSPD. The motion of the laser beam spot is detected via the voltage change in the photodetector quadrants, and the change in the vertical direction is used to keep the tip – sample distance constant by feedback control, while the change in the horizontal direction can be converted to the lateral force experienced by the tip by a method which will be discussed later in this section.

- Piezoelectric actuators are used for various purposes in AFM. As mentioned before, to achieve raster scanning of the sample relative to the tip, piezoelectric actuators are used. Also, to control the tip – sample distance in the vertical direction, one of the most common techniques is to use piezoelectric actuators, where it would act as the actuator in the feedback control setup. Another use of piezoelectric actuators in AFM is as a shaker, which is the name for the piezoelectric actuator used to vibrate the cantilever in oscillatory imaging modes.
- The final main element of the AFM is the proportional – integral (PI) feedback controller, which is used to keep the tip – sample distance constant during scanning. The controller takes the input signal (caused by deflection of the cantilever in the vertical direction due to bending by normal forces) from the PSPD, and during scanning, tries to keep this signal (and thus, the tip – sample distance) at a constant value set by the user. This is achieved by feeding an output signal into the piezoelectric actuator that adjusts the tip – sample distance, and the amount of piezo displacement (in the vertical direction) needed to keep this distance constant is recorded as sample topography. Additionally, the detected deflection of the cantilever in the vertical direction can be converted into normal force by multiplication with the cantilever stiffness,  $k$ .

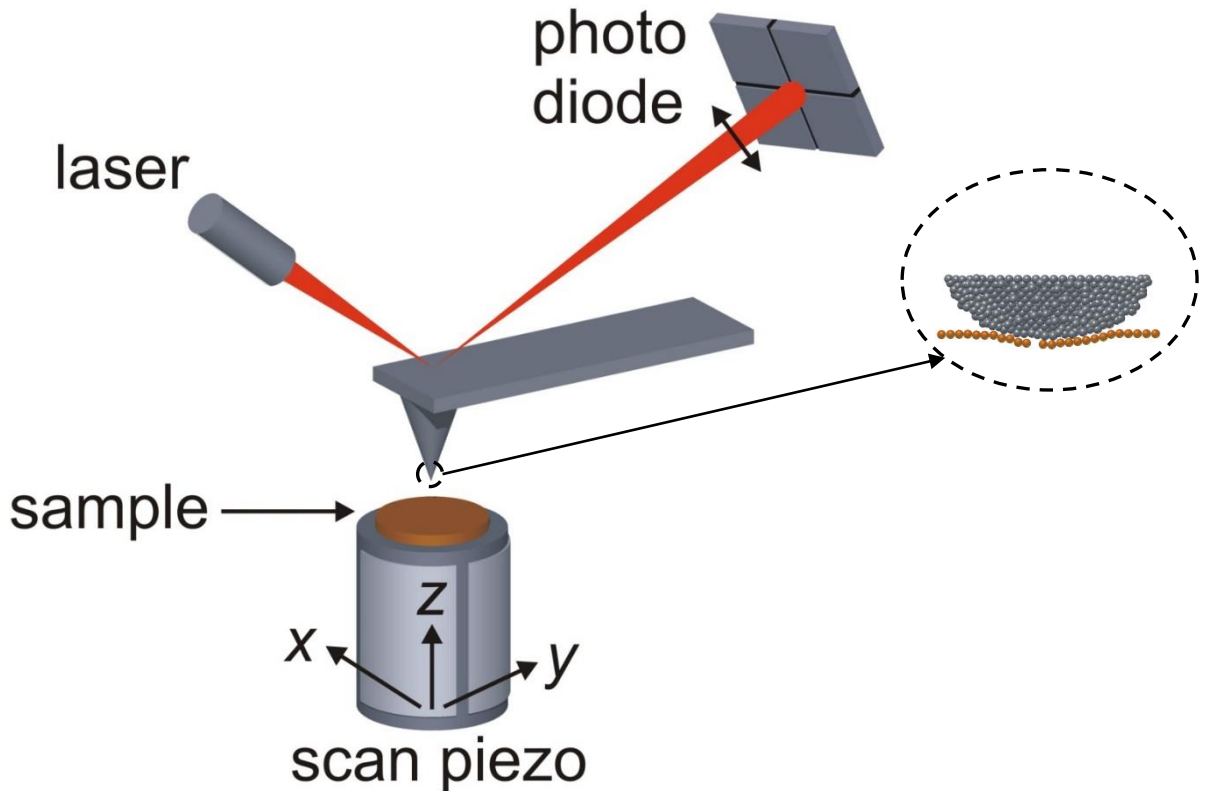


**Figure 2.9** Schematic of the AFM setup, and the sketch of the AFM tip, which is considered as a single asperity contact. Adapted from [37].

AFM can be used in various modes depending on the application. The most common modes are contact mode and tapping mode, but for specific applications, modes like Kelvin probe force microscopy, noncontact atomic force microscopy and magnetic force microscopy can be used, to name a few. Contact mode AFM (C-AFM) is the first AFM mode developed [38] and also the method of choice for this work. As explained above, in C-AFM, a flexible cantilever is used to scan the surface while keeping the tip – sample distance constant by setting a constant normal force (or, in other words, cantilever deflection) value. The reason to use a flexible cantilever, meaning a cantilever with a lower  $k$ , is to increase the amount that the cantilever would deflect under a certain load, and thus to increase sensitivity. To keep the distance constant, the PI controller takes the deflection signal from the PSPD and “corrects” the distance by feeding corrected output signals to the vertical piezo actuator. These corrected signals are used to determine the topography of the sample. In C-AFM, parameters that can be modified by the user are the scan speed, which corresponds to the rate by which each line is scanned, normal force, which determines

the set distance of the tip relative to the sample and control parameters (P and I). These parameters are set by the user to maximise image quality. Limits of the scan speed depend on the instrument, and after a certain threshold, the tracking error of the controller will increase. Normal force is set according to the characteristics of the sample and the experiment. In general, increasing the normal force will increase the image quality, since the tip is in more intimate contact with the sample; but this should be done carefully, since it might lead to sample damage and wear, and also the rate by which the tip loses its sharpness will increase. Finally, control parameters are adjusted in such a way that the user will keep increasing the gain values up to the point where feedback oscillation occurs and then stay a little bit below this value.

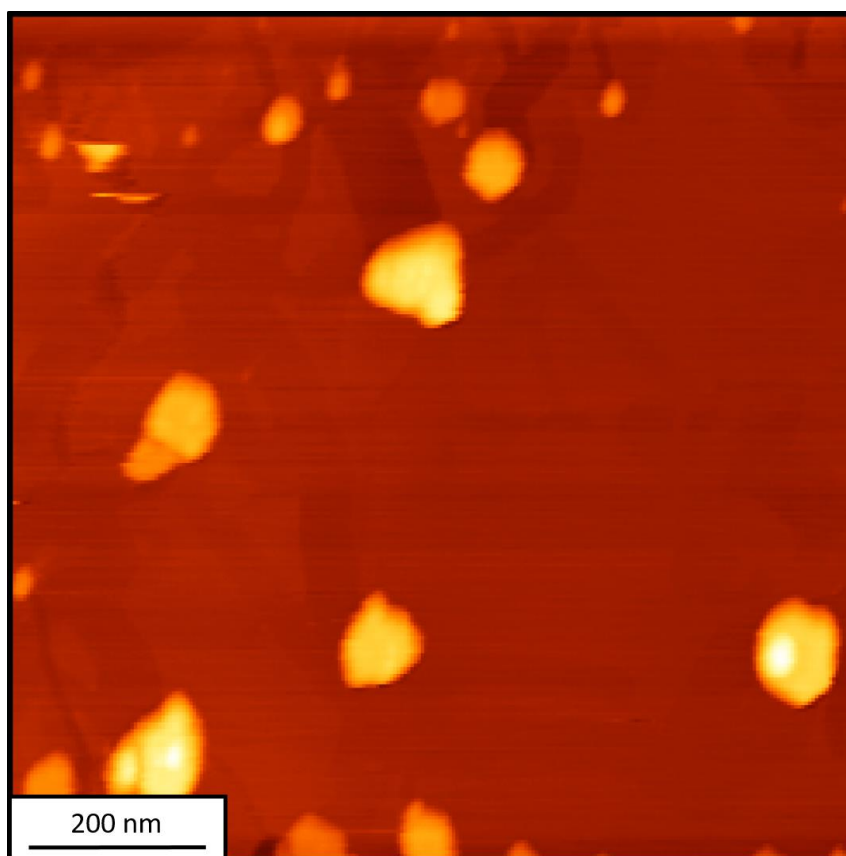


**Figure 2.10** Contact mode AFM image of platinum nanoparticles deposited on graphite.

In tapping mode AFM, i.e. intermittent contact AFM, the cantilever is oscillated by the shaker piezo, and the change in amplitude, which is caused by surface forces, is taken as the main signal for the feedback control loop. The feedback is optimized such

that tip touches the surface only during the peak of the oscillation. The parameters that can be modified in this method are the oscillation frequency, scan speed, control parameters and the amplitude set point. Scan speed and control parameters are adjusted in the same manner as C-AFM. Oscillation frequency is determined to be near the resonance frequency of the cantilever. Stiffer cantilevers than C-AFM are preferred, since the resonance frequency of these cantilevers are higher; in other words, better from a thermomechanical noise perspective. The amplitude set point is the maximum decrease allowed for the amplitude signal, which is a result of the force experienced by the tip during interaction with the surface. Increasing this value will increase the tip – sample interaction, similar to the set normal force in C-AFM.

Both C-AFM and tapping mode AFM can be used in vacuum, ambient conditions or liquid. This makes these two modes quite popular; also more specific AFM modes such as friction force microscopy, electrostatic force microscopy and magnetic force microscopy are based on these operation modes. Both modes have advantages and disadvantages over each other, and these have to be considered when choosing the mode of operation in measurements. In C-AFM, the tip is always in contact with the sample, which allows both to measure lateral forces and apply forces to the surface continuously. However, in the case of soft or vulnerable samples, e.g. biological samples, this would cause damage to the sample, so tapping mode AFM is a better operation mode for imaging such samples. In the case of AFM operation under ambient conditions, there is always a capillary water layer on the surface, which creates additional adhesion between the tip and the sample. In tapping mode AFM, the restoring force of the cantilever pushes the cantilever out of the capillary layer, eliminating effects of the layer on the image. Lastly, in the case of imaging in liquids, when a piezo shaker is used to oscillate the cantilever in tapping mode, vibrations will travel through the fluid medium, creating additional oscillations, and also the quality factor will drop significantly due to the factor that oscillations take place in a more viscous medium. In the case of the experiments conducted in this thesis, the C-AFM mode is used, in order to be able to manipulate the nanoparticles by pushing with the AFM tip and to simultaneously measure the lateral forces which are related to the friction experienced by the nanoparticles during manipulation.

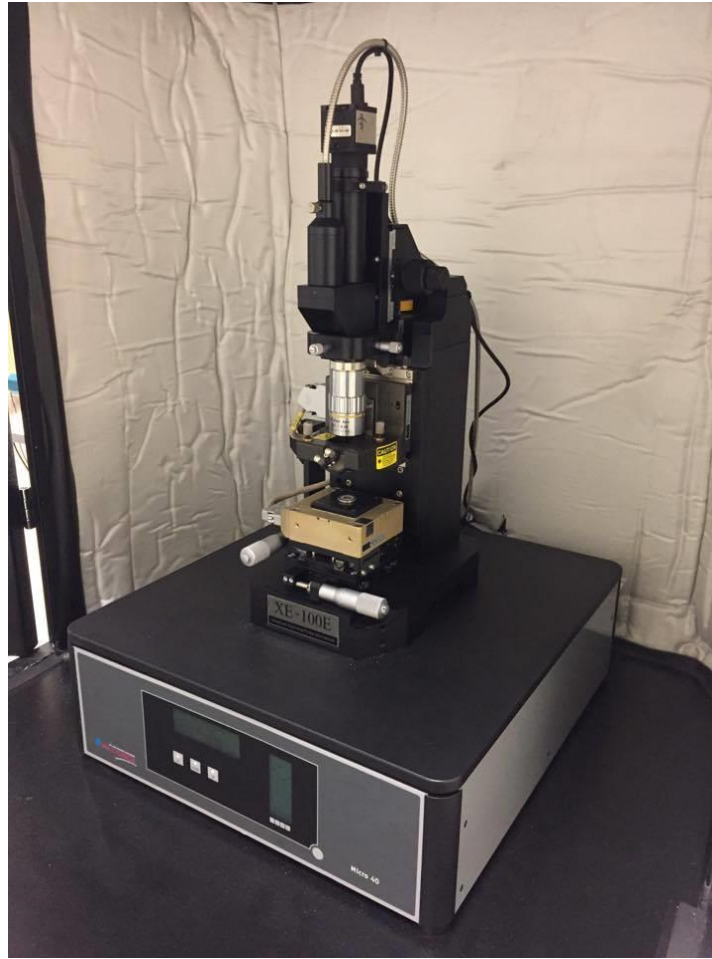


**Figure 2.11** PSIA XE-100E AFM used for the experiments presented in this work.

#### **2.4.1 Friction Force Microscopy**

Friction Force Microscopy (FFM), as previously mentioned, is a variation of AFM, where the displacements of the laser beam spot on the PSPD in both vertical and horizontal directions are taken into account. One of the first implementations of this technique as a variation of AFM has been done by Meyer et al. in 1990 [39]. In this method, the AFM is operated in contact mode, and while the laser displacement signal in the vertical (normal) direction is used exactly in the same fashion as C-AFM, the laser displacement signal in the horizontal (lateral) direction is also recorded, which corresponds to the torsional twisting of the cantilever, a result of lateral forces acting on the tip. However, during scanning on an actual sample surface, the friction force experienced by the tip is not the only lateral force acting on the cantilever: When the tip encounters a height difference in the sample, the tip will deflect laterally due to

repulsive force components in the lateral direction. This causes a cross-talk between the lateral and normal signals (Figure 2.12). To detect and correct for such cross-talk, both topography and lateral force images should be taken simultaneously [40]. As friction force acts in the opposite direction to the motion, forward and backward scans of the lateral force will give voltage values with reverse signs. By plotting forward and backward scans of the same line, a *friction loop* is obtained. To eliminate cross-talk between normal and lateral signals, and to obtain an absolute value for the friction force, the friction loop half-width ( $w$ ) is used for friction analyses. A schematic of a representative friction loop can be seen in Figure 2.13.

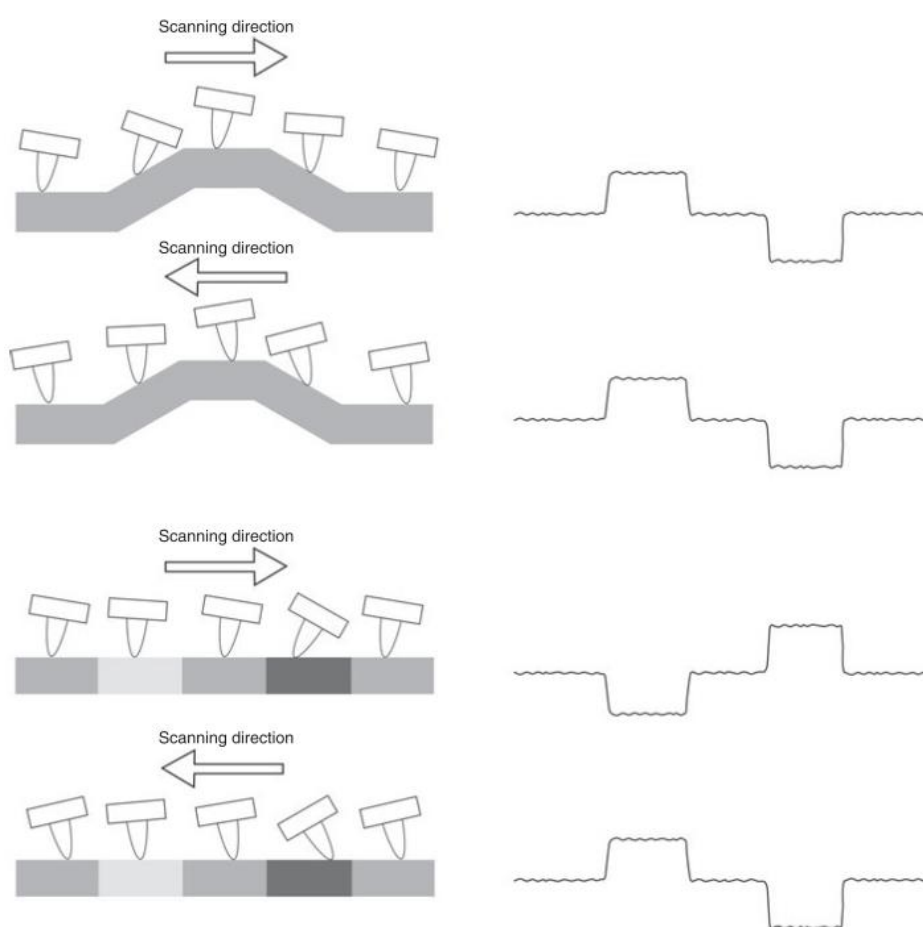


**Figure 2.12** Schematics of several model sample surfaces are shown on the left and recorded lateral force signals on the right. Surface regions with darker colors correspond to higher coefficients of friction. As one can easily see, a change in height (but not in friction coefficient) would cause the cantilever to torsionally twist in the same manner as it would upon a change in friction coefficient, and result in an artificial “friction signal”. Adapted from [38].

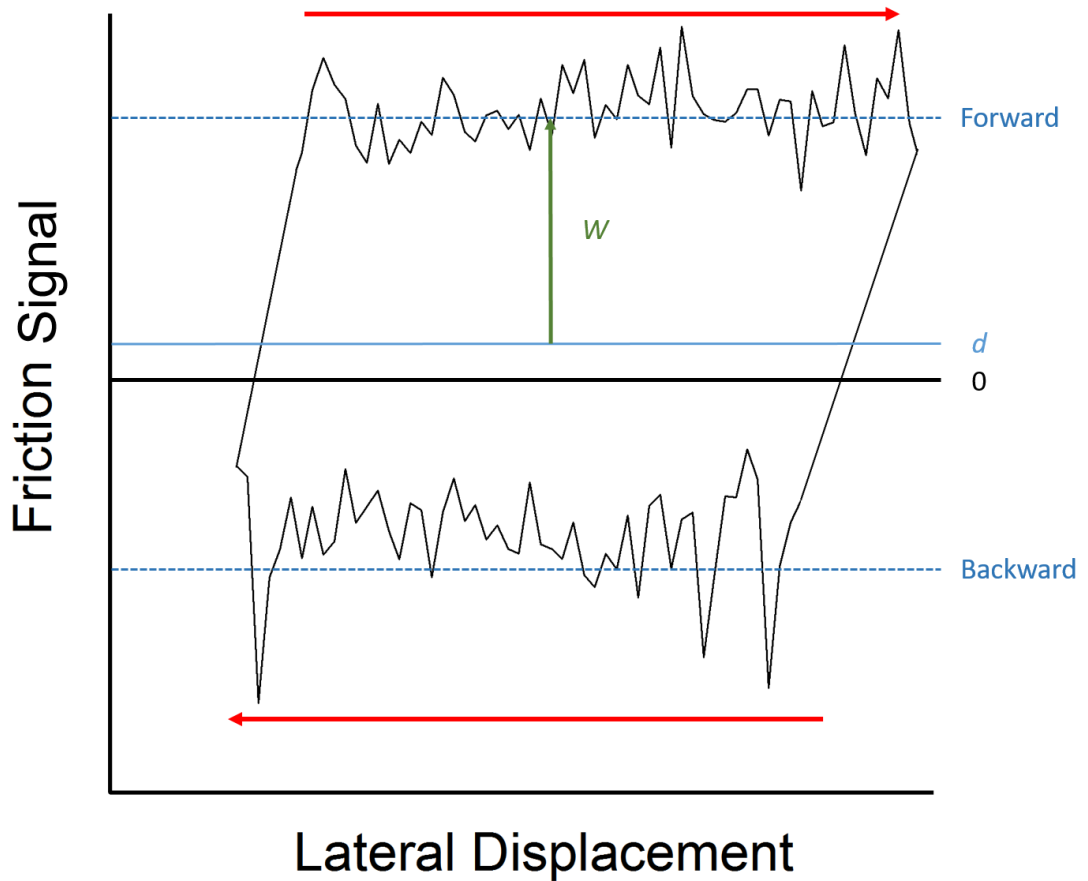


**Figure 2.13** Schematic of a friction loop, where the friction loop half-width is denoted by the green arrow and the offset from zero is denoted with the full, light blue line. Dashed blue lines show mean signals in the forward and backward scanning directions.

#### 2.4.2 Cantilever Calibration

Although the name AFM infers that force is a directly measured quantity in AFM, this is not the case as the forces are derived from the elastic deformations of the cantilever. To convert these deformation signals (deflection and twisting) into force, the stiffness of the cantilever in the normal direction as well as the lateral force calibration factor have to be determined. To determine the bending stiffness  $k$  of the cantilever, a very common method is used in this thesis, namely the so-called *Sader method* [41]. In this method, the geometric properties of the cantilever along with its resonance frequency are used to determine its stiffness.

The formula proposed in this paper is:

$$k = M_e b h L \rho_c \omega_{vac}^2 \quad (2.3)$$

where  $k$  is the stiffness of the cantilever,  $M_e$  is the effective mass of the cantilever, which is a function of cantilever aspect ratio that converges to 0.2427 in the case of  $L/b > 5$  (as is the case for the cantilevers used for the experiments here),  $b$ ,  $h$ , and  $L$  are the width, length and thickness of the cantilever, respectively, and along with  $\rho_c$ , density of the cantilever material, constitute the mass of the cantilever. In the case of cantilevers used in this thesis, these values are 50  $\mu\text{m}$ , 2  $\mu\text{m}$ , 450  $\mu\text{m}$ , and the density is taken as the density of the silicon, which is 2329  $\text{kg/m}^3$ . Lastly,  $\omega_{vac}$  is the angular resonance frequency of the cantilever in vacuum. Since the experiments are conducted under ambient conditions, a correction for this formula is used, which results in a 4% increase in stiffness [41]. By using the Sader method, it was found that the cantilevers used for the experiments here have stiffness values ranging from 0.09 N/m to 0.25 N/m. To convert the vertical deflection into force, Hooke's law is used, which states

$$F = k x \quad (2.4)$$

where  $x$  is the vertical displacement, and by simply multiplying with bending stiffness  $k$ , it can be converted to force.

Lateral calibration of AFM cantilevers is more tedious than the normal force calibration, since the underlying mechanisms of bending and torsion for the beams are different, and factors other than the lateral stiffness are taken into account in calibration. There are several methods proposed for lateral calibration in AFM, such as the lever method, axial sliding method, torsional added mass method and wedge method [42]. In this work, an improved wedge calibration method proposed by Varenberg *et al.* is used [43]. In this method, a calibration sample that has wedges with well-defined angles is used, such as the MikroMasch TGF 11 silicon calibration grating suggested by the authors (Figure 2.14). The calibration sample is scanned by the AFM tip along the wedges and lateral deflection images from both forward and backward scans are gathered to obtain friction loops. These friction loops are collected with normal force set points ranging from 0.5 nN to 5 nN, in a way to make a

continuous data point set (i.e. 10 data points with 0.5 nN intervals). From these friction loops, friction loop half-width ( $w$ ) and friction loop offset ( $d$ ) values for each normal force are obtained. These are used to calculate the lateral force calibration factor  $\alpha$  via equations:

$$\alpha w_0 = \frac{\mu}{\cos^2 \theta - \mu^2 \sin^2 \theta} \quad (2.5)$$

$$\alpha d_0 = \frac{(1 + \mu^2) \sin \theta \cos \theta}{\cos^2 \theta - \mu^2 \sin^2 \theta} \quad (2.6)$$

where  $\alpha$  is the lateral calibration constant with units nN/V,  $\mu$  is the coefficient of friction,  $\theta$  is the angle of the wedges, which is  $54^\circ 44'$  for the employed calibration grating, and  $d_0$  and  $w_0$  are the slopes of  $d$  and  $w$  with respect to normal force. By solving these two equations with two unknowns, namely  $\alpha$  and  $\mu$ , the lateral force calibration factor can be easily found. This procedure is used for both the upward slope and the downward slope of the wedge, and the average of these two calculations are taken as the lateral calibration factor. After  $\alpha$  is obtained, lateral signals measured in Volts can be converted to forces by multiplying with the lateral calibration factor  $\alpha$ . For the AFM tips used in our experiments, this factor had a range from 4.39 nN/V to 28.3 nN/V.

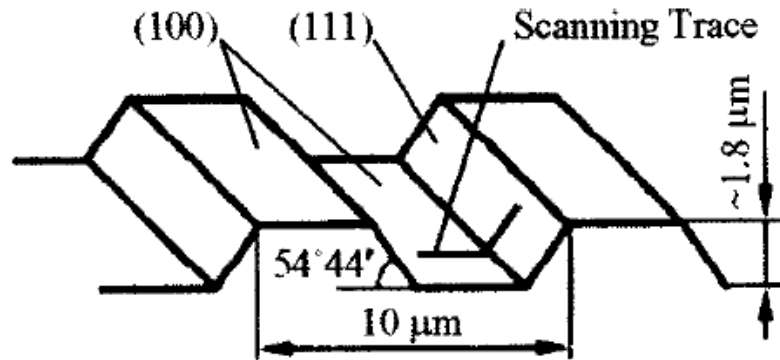


**Figure 2.14** Schematic drawing of the MikroMasch TGF11 lateral force grating used for lateral calibration. (100) and (111) refer to the crystallographic planes of Si. Taken from [43].

# Chapter 3

## Sample Preparation and Characterization

### 3.1 Sample Preparation

As already introduced in Section 1.2, nanotribology experiments can be conducted by means of manipulating nanoparticle sliders on flat substrates via AFM. In this thesis, platinum and platinum oxide nanoparticle sliders on highly oriented pyrolytic graphite (HOPG) are employed towards this purpose. This section details the preparation of these samples.

#### 3.1.1 Preparation of Platinum Nanoparticles

Platinum nanoparticles are obtained by a process which involves several steps. First, a fresh HOPG surface is obtained by mechanically cleaving a bulk HOPG sample via mechanical exfoliation using common Scotch Tape. The HOPG sample is then immediately put under high vacuum ( $\sim 10^{-5}$  Torr) in an e-beam evaporator, which is subsequently used to deposit platinum on the surface. E-beam evaporation is a physical vapour deposition technique that employs high energy electron beams to vaporize the material to be deposited in a high vacuum chamber. The vapour will then

precipitate inside the vacuum chamber which includes the sample, thus coating the sample. The thickness of the deposited material and the rate of deposition are measured by the change of resonance frequency of a quartz crystal micro-balance and controlled by the electron beam current. The thickness of the desired layer is initially calibrated for different materials, and the user can afterwards set the desired film thickness for a given material before the deposition.



**Figure 3.1** Vaksis MIDAS E-Beam evaporation system used for sample preparation.

Since it is desired to produce nanoparticles, and not a continuous thin film in this thesis, a minimal film thickness of 1 nm and the lowest possible deposition rate (1 Å/s) have been used as parameters for evaporation. This results in an imperfect film with low surface coverage, as seen in Figure 3.2. The main reason to choose E-Beam evaporation over other physical vapour deposition (PVD) methods, e.g. thermal evaporation, is that currently available PVD devices in UNAM other than E-Beam evaporation either lack the power required to evaporate platinum or are incapable of creating imperfect thin films which will be subsequently annealed into platinum nanoparticles with desired sizes. PVD methods are chosen over chemical vapour deposition (CVD) methods in order to avoid chemical modification of the nanoparticle and substrate surfaces.

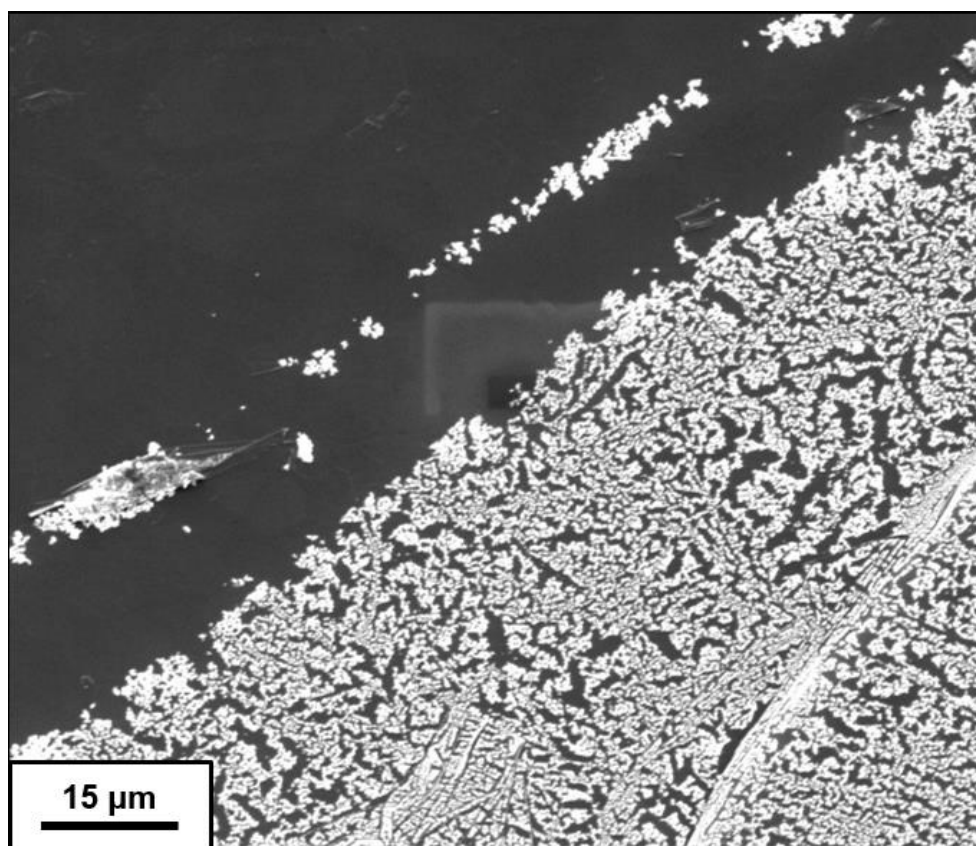


**Figure 3.2** Large-scale SEM micrograph of platinum deposited on a clean HOPG surface via e-beam evaporation.

After the deposition of platinum on HOPG, samples are subjected to a post-deposition annealing process, which has been previously shown to produce crystalline nanoparticles from imperfect gold thin films [44]. For this process, a rapid thermal annealing (RTA) system is used (Figure 3.3). Samples are annealed at 1000 °C for 30 minutes, which results in platinum nanoparticles with various sizes (up to a few hundred nm in lateral dimensions), as seen in Figure 3.4. It should be mentioned that these parameters as well as the parameters for E-beam evaporation have been optimized via many trials until platinum nanoparticles of desired size, shape and distribution have been obtained.



**Figure 3.3** Rapid thermal annealing (RTA) system used to prepare samples.

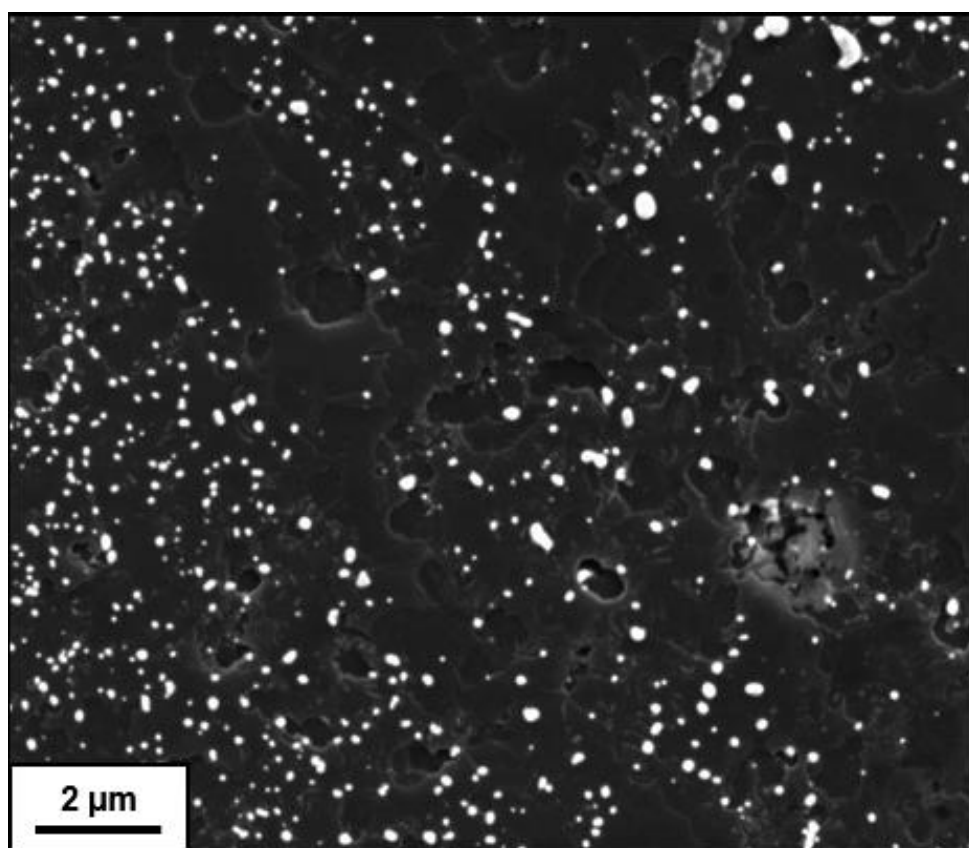


**Figure 3.4** Large-scale SEM micrograph of the HOPG surface decorated with platinum nanoparticles after post-deposition annealing.

### 3.1.2 Preparation of Oxidised Platinum Nanoparticles

Oxidised platinum nanoparticles are prepared using the same method as the platinum nanoparticles, with an additional step. First, the oxidation of platinum under ambient conditions has been tested by leaving platinum samples exposed to air for several months. Although XPS results from these samples showed an increase in oxygen content (most likely due to the adsorption of organic molecules from the ambient), no significant change in platinum spectra (and thus no oxidation of platinum) has been detected. Instead, a method proposed by Li *et al.* has been used to obtain oxidised platinum nanoparticles, which involves the exposure of platinum nanoparticles to oxygen plasma generated in a reactive ion etching (RIE) system [45]. For this purpose, the Leybold LE 301 RIE system in ARL is used. In this system, the sample is first inserted into a vacuum chamber, which is subsequently filled with oxygen. By applying a strong radio frequency electromagnetic field to the sample plate, the gas is ionised and converted into the plasma state. The user can determine the gas pressure in the chamber, power of the electromagnetic field and duration of the process. These parameters have been optimized (50  $\mu$ Bar, 50 W, 2 minutes, respectively) in order to oxidise the nanoparticles without changing their morphology significantly. Sample SEM images of over-exposed and optimally oxidised nanoparticles can be seen in Figure 3.5.

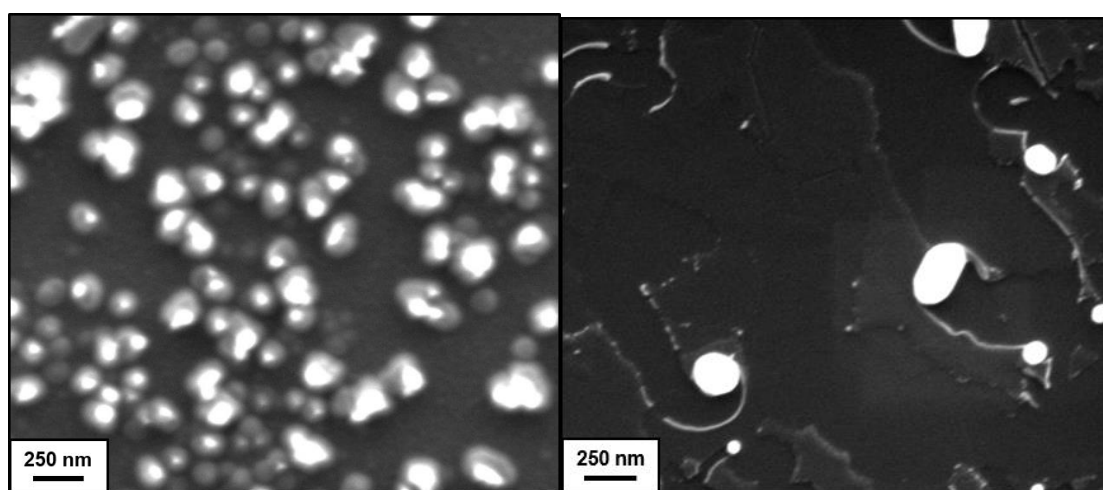


**Figure 3.5** SEM micrographs of over-exposed platinum nanoparticles (left) and platinum nanoparticles oxidised with optimal parameters (right).

## 3.2 Sample Characterization

### 3.2.1 Structural Characterization via SEM and TEM

In order to investigate structural lubricity, nanoparticles that feature crystalline structure all the way to their surfaces (i.e., the absence of an amorphous oxide layer on the surfaces) are needed. To make sure that this is the case, structural and chemical characterization of the nanoparticles have to be carried out. Structural characterization of the nanoparticles is performed via SEM and TEM in this thesis. SEM is used to confirm nanoparticle formation and structural characterization. After each preparation step, SEM micrographs (such as those in Figure 3.2, Figure 3.4 and Figure 3.5) are taken to optimize sample preparation parameters. It can be seen in Figure 3.4 that after post-deposition annealing, nanoparticles with various sizes are formed. Also, the distribution of the nanoparticles is wide enough to conduct manipulation experiments on individual particles, and close enough to do so in a 10  $\mu\text{m}$  x 10  $\mu\text{m}$  square, which is the maximum AFM scan size used in the experiments. The effect of plasma oxidation on nanoparticle morphology can also be observed via SEM, and the oxidation parameters are optimised accordingly. It can be seen in Figure 3.5 that over-exposure causes significant changes in nanoparticle morphology while oxidation under optimised parameters does not. Another aspect to notice is that after post-deposition annealing, graphite in the vicinity of the nanoparticles is etched down, forming grooves (Figure 3.4). This is attributed to thermally activated etching of graphite by metal nanoparticles, as discussed previously [46].

To confirm the crystallinity of the nanoparticles and the atomic flatness of the sliding surfaces, TEM studies are conducted. TEM samples are prepared by scraping the platinum-nanoparticle-deposited HOPG surface into 0.8 ml ethanol and then sonicating the solution. This solution was then drop-cast onto a copper TEM grid. By using TEM, it was observed that nanoparticles have well-defined facets, leading to the conclusion of a crystalline structure (Figure 3.6). Additionally, HRTEM micrographs clearly show crystallographic planes, which provides another confirmation for crystallinity (Figure 3.6). Selected area diffraction patterns gathered from the nanoparticles show single spots characteristic of single crystal structure (Figure 3.7).

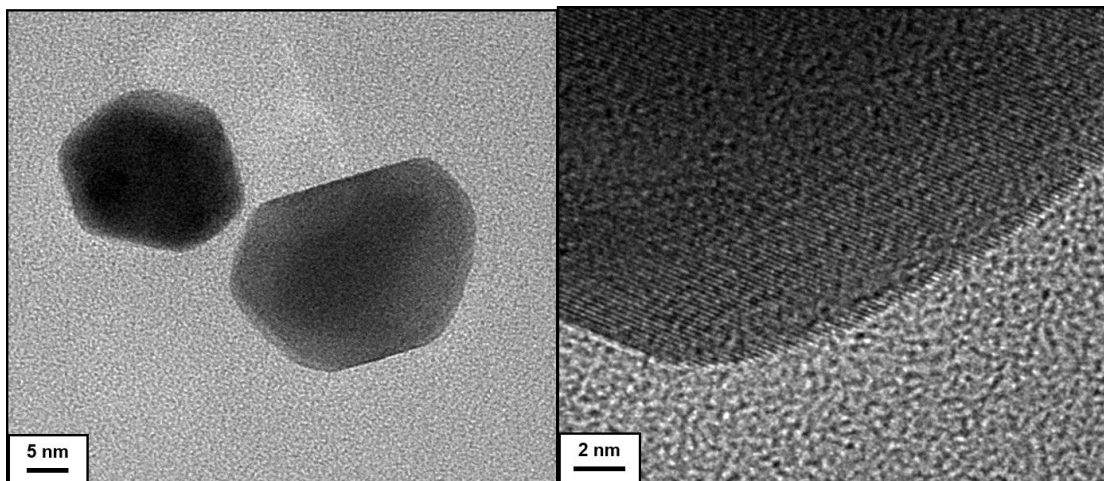


**Figure 3.6** Bright field TEM (left) and HRTEM (right) micrographs of platinum nanoparticles.

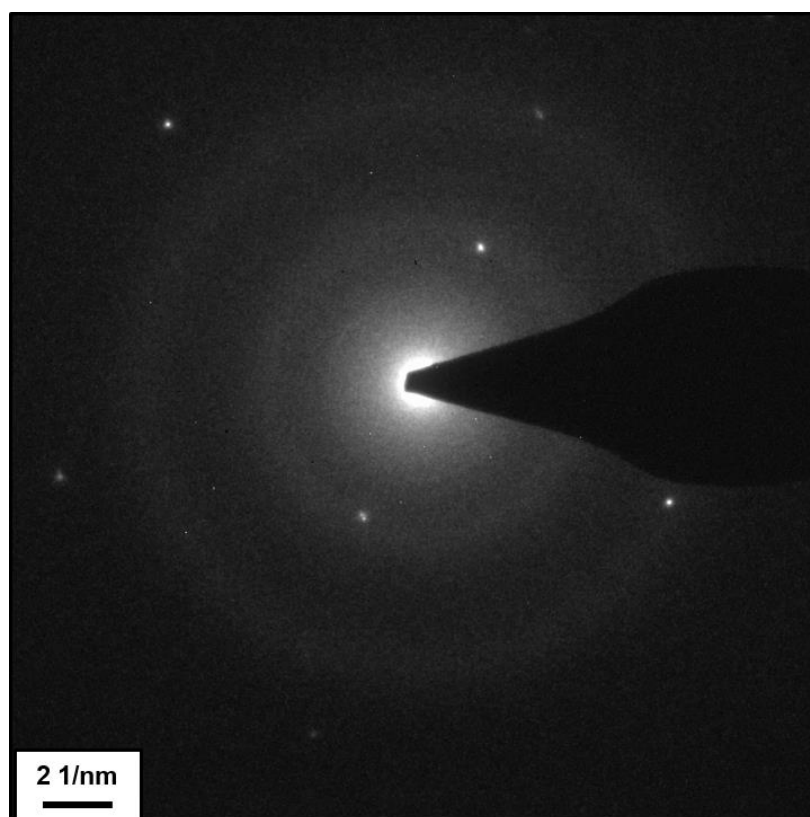


**Figure 3.7** Selected area diffraction pattern gathered from platinum nanoparticles.

For further structural characterization, cross-sectional TEM is used. Towards this purpose, samples are prepared by coating the top (platinum-deposited) layer of the HOPG by epoxy compatible with focused ion beam (FIB) milling (Micro Measurements M-Bond 610), and then cutting a thin slice ( $\sim 10$  nm) by FIB milling, which is then welded onto an Omniprobe TEM grid by platinum welding. Cross-sectional TEM micrographs seen in Figure 3.9 show that continuous atomic planes are stacked from the bottom (sliding) surface all the way to the top surface in a parallel manner. Spacing between the planes agree with the expected inter-planar spacing of platinum (111) planes ( $2.26 \text{ \AA}$ ). From these images, it can be deduced that the sliding surface is indeed atomically flat, and the surfaces exposed to air are free from amorphous oxide layers, thus being suitable for structural lubricity experiments.

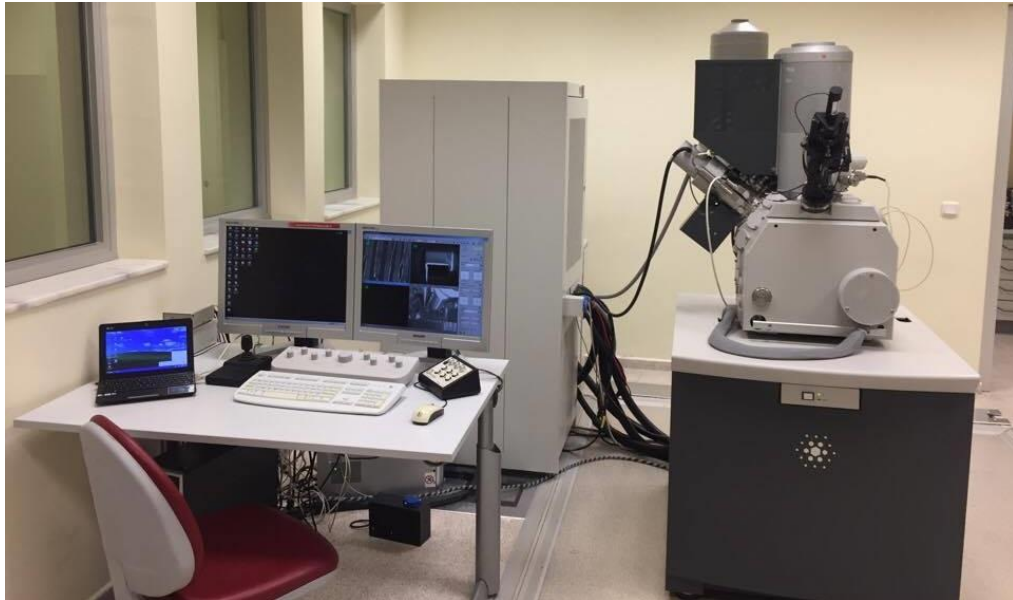


**Figure 3.8** FEI Nova 600i Nanolab FIB device used to prepare cross-sectional TEM samples.

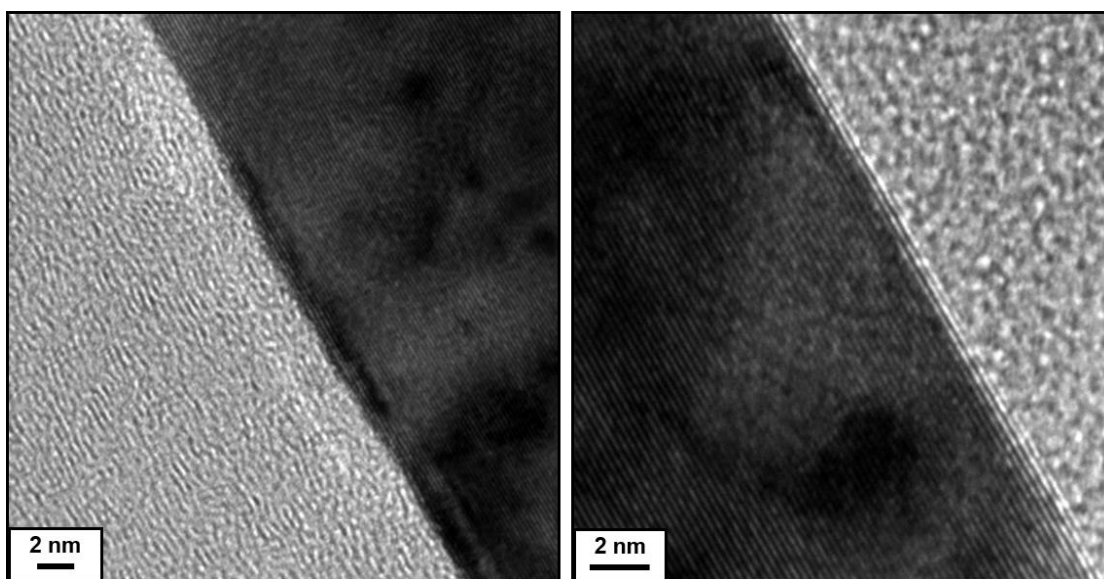


**Figure 3.9** Cross-sectional TEM micrographs taken from the bottom (sliding) surface (left) and the top surface (right) of a platinum nanoparticle. Top side of the left image is platinum, and the bottom side is graphite. Top side of the right image is epoxy, and the bottom side is platinum. Atomic planes of platinum proceeding all the way to the top and bottom surfaces, as well as the absence of an amorphous oxide layer, are clearly observed.

For the structural characterization of oxidised platinum nanoparticles, cross sectional TEM images were taken, as seen in Figure 3.10. However, due to the large thickness of the samples prepared via FIB and the fact that they feature an oblique shape leading to a tilt angle with respect to the incident electron beam (which potentially causes signals from different portions of the sample such as epoxy, platinum, graphite, and platinum oxide to overlap), structural analysis of the images was inconclusive. In the left and right micrographs in Figure 3.10, the effect of this overlap can be seen as the atomic planes with different orientations interfere with each other, leading to the observation of hexagonal patterns.

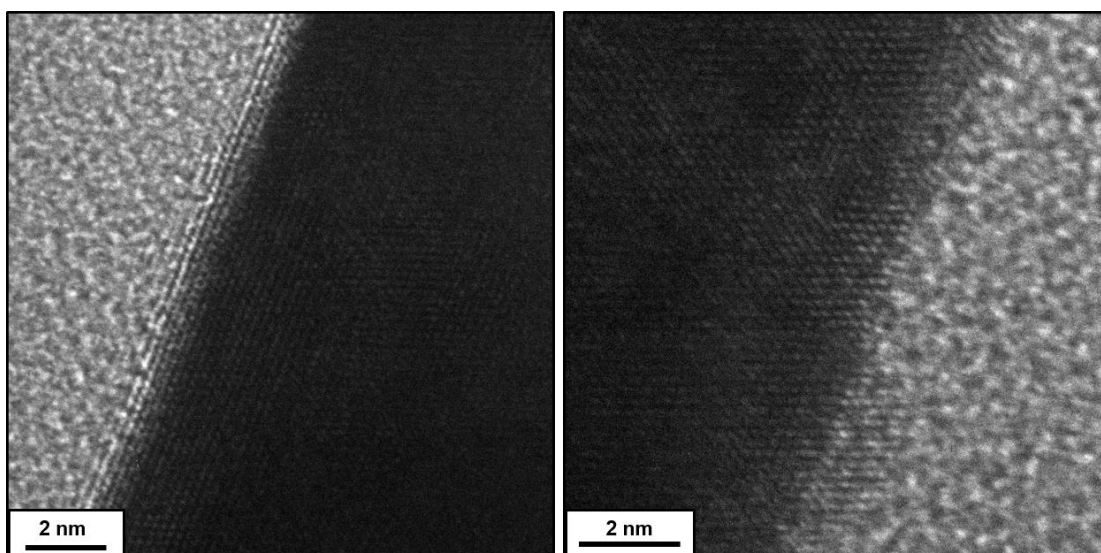


**Figure 3.10** Cross-sectional TEM micrographs taken from the bottom (sliding) surface (left) and the top surface (right) of an oxidised platinum nanoparticle. Top side of the left image is graphite, and the bottom side is nanoparticle. Top side of the right image is nanoparticle, and the bottom side is epoxy. The hexagonal patterns are caused by the tilted angle of the sample with respect to the incident electron beam.

### 3.2.2 Chemical Characterization via XPS

Chemical characterization of the nanoparticles is of great importance, since chemical structure of the sliding surfaces has significant effects on friction, as stated in Chapter 1. For chemical characterization purposes, X-ray photoelectron spectroscopy and energy dispersive X-ray spectroscopy are used. XPS spectra taken from platinum nanoparticles on HOPG can be seen in Figure 3.11. Here, a wide survey from 0 eV to 1350 eV shows three peaks, one near 75 eV, one near 284 eV and another one near 535 eV. The step at 1230 eV is associated with the Auger electron peak of carbon, and confirms the existence of carbon on the sample. Narrow spectra taken between 64-87 eV, 278-297 eV and 525-545 eV show the structure and the positions of the peaks detected in the survey spectrum. These intervals are specific to Pt4f, C1s and O1s orbital energy levels, respectively. In the Pt spectrum, two peaks with a spin-orbit splitting of 3.35 eV, characteristic to Pt 4f peaks, is visible. Doublet peaks are a characteristic of f peaks, and in this case peak positions of 71.3 eV and 74.6 eV agree with the reference values [47]. This spectrum shows that platinum is in its elemental state, meaning there are bonds made among platinum atoms. In the C spectrum, the

C1s peak, which is the most intense peak in the whole spectrum, is at 284.5 eV, and upon comparison with the reference, which states the C1s peak position at 284.6 eV, all recorded spectra have been shifted by 0.1 eV for correction. There is also a vague but visible peak at 291 eV, which is attributed to C–O bonds, hinting at the existence of organic contaminant molecules on the surface. In the O spectrum, the O1s peak at 532 eV can be seen, and it can also be observed that the spectrum potentially consists of multiple peaks; however determination of these peaks could not be done. The reason behind this is that the molecular orbital energy levels of O are very close (in the range of  $\sim 0.4$  eV) and distinguishing different peaks requires a careful curve fitting process which is outside of the scope of this thesis.

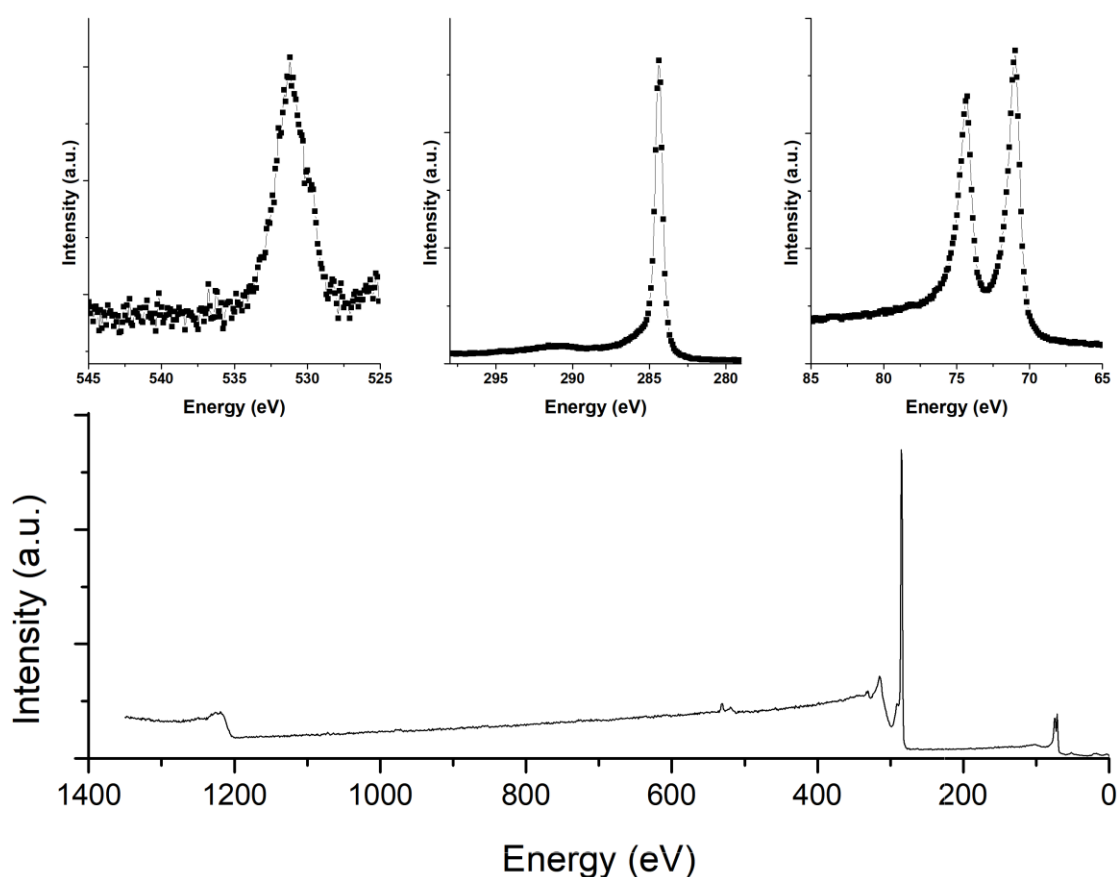


**Figure 3.11** XPS spectra taken in specified energy ranges from Pt nanoparticles deposited on HOPG. Top left: O range (525-545 eV); top middle: C1s range (278-297 eV); top right: Pt4f range (64-87 eV); bottom: wide survey.

XPS spectra shown in Figure 3.12 are taken from oxidised platinum nanoparticles on HOPG. In the survey spectrum, compared to the survey spectrum in Figure 3.11, the

intensity of the oxygen peak is significantly higher, while the carbon spectrum is fairly similar (C1s peak at 284.5 eV). Also the Auger line of oxygen can be seen at ~980 eV, which can be barely seen in the non-oxidised sample. This increase in the oxygen peak intensity is expected, as the sample is treated with oxygen plasma. The most significant difference between the two measurements is in the platinum spectra, where in the oxidised case there is a third peak appearing in the spectrum. This points out that there is a change in the electronic structure of platinum, and is an indicator of Pt-O molecular orbital [48]. From this observation, it can be concluded that the RIE oxidation process has indeed been successful in oxidising platinum nanoparticles.

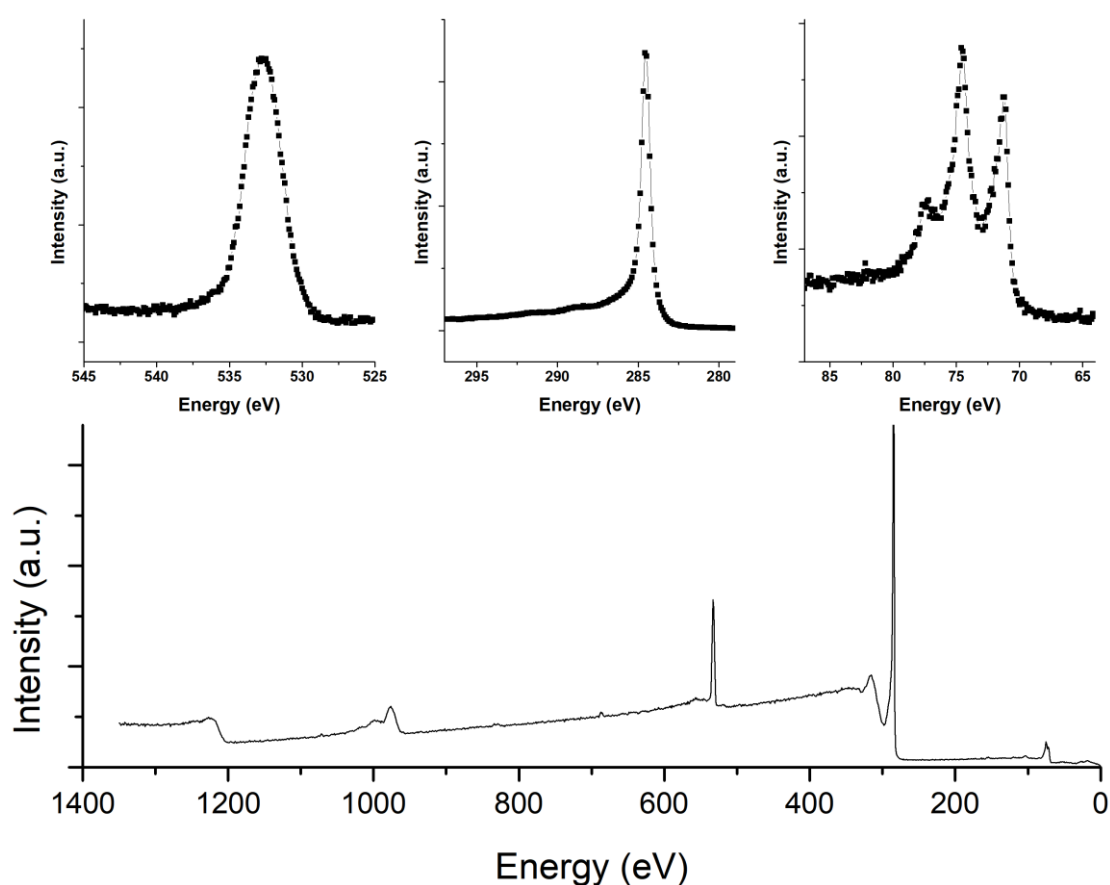


**Figure 3.12** XPS spectra taken from oxidised platinum nanoparticles deposited on HOPG. Top left: O range (525-545 eV); top middle: C1s range (278-297 eV); top right: Pt4f range (64-87 eV); bottom: wide survey.

A more quantitative analysis of the oxidised platinum spectrum is conducted both in order to support the confirmation of the oxidation and to find out the structure of the oxide, as platinum typically forms two oxide compounds: PtO (platinum(II) oxide or

platinum monoxide) and PtO<sub>2</sub> (platinum(IV) oxide or platinum dioxide). To perform this analysis, data taken from the spectrometer are processed via *XPSpeak 4.1*. To conduct a peak fitting session in order to determine the number of peaks and their positions in the spectrum, the signal background has to be removed. There are several methods to determine the background signal in an XPS spectrum, e.g. Shirley and Tougaard methods, and in this analysis, the Shirley background method is used. After the background is removed, peaks with predefined properties specific to platinum (orbital type, spin-orbit splitting) are fitted through Newton's method with peak position, peak area and peak full-width half maximum parameters. The result of this analysis is shown in Figure 3.13. Here, the black line is the raw data, violet line is the removed background, blue, dark blue and red lines are fitted curves, and the dark green line is the sum of the peaks, which fits the raw data precisely. The blue doublet peaks, where the peak with the lower binding energy is positioned at 71.2 eV, are attributed to Pt 4f peaks that have a spin-orbit splitting of 3.35 eV, and the dark blue doublet peaks are a characteristic of the platinum spectrum, again attributed to elemental platinum [48]. The lower energy peak of the red doublet peaks that originate after the oxidation is positioned at 74 eV. To confirm the structure of the oxide, a comparison with reference data was performed, and the results can be seen in Table 3.1. C1s peak positions are added to the table to normalize the peak positions, so that there will be a 0.5 eV shift in the comparison. Peak positions of elemental platinum coincide perfectly with the reference, and it can be seen that there is only a 0.1 eV difference between the oxide peak in the spectrum and the PtO peak position in the reference. From this comparison, it can be deduced that the oxidised platinum in our experiments is in the form of PtO.

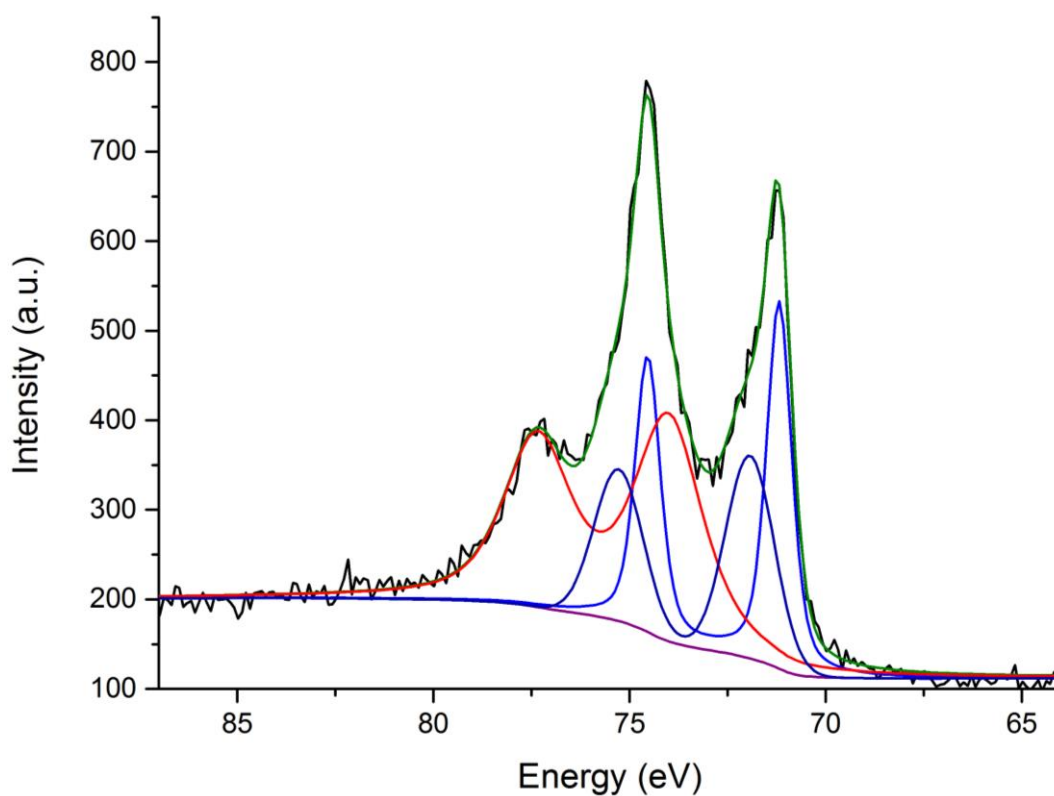


**Figure 3.13** Peak-fitted XPS data taken from oxidised platinum nanoparticles deposited on HOPG.

**Table 3.1** Comparison of experimental spectrum peak positions of Figure 3.13 and reference peak positions

Orbitals	Peak Positions (eV)	
	<i>Experimental Results</i>	<i>Kim et al. [48]</i>
<b>C1s</b>	284.5	284
<b>Pt4f</b>	71.2	70.7
<b>PtO4f</b>	74	73.4
<b>PtO<sub>2</sub>4f</b>	-	74.2

To determine the oxygen distribution inside oxidised platinum nanoparticles, EDX measurements along with HAADF images are taken via TEM. In Figure 3.14, the cross-sectional HAADF TEM image of an oxidised platinum nanoparticle, along with an EDX line profile taken for oxygen, is shown. The profile is taken in the direction of the yellow arrow, and it can be seen that the sliding surface has less oxygen content than the exposed surface, as expected. An EDX map taken on the same nanoparticle can be seen in Figure 3.15. Here, the map shows that both the top surface of the nanoparticle and the sides (which are also exposed to oxygen plasma) feature more oxygen content than the bottom (sliding) surface.

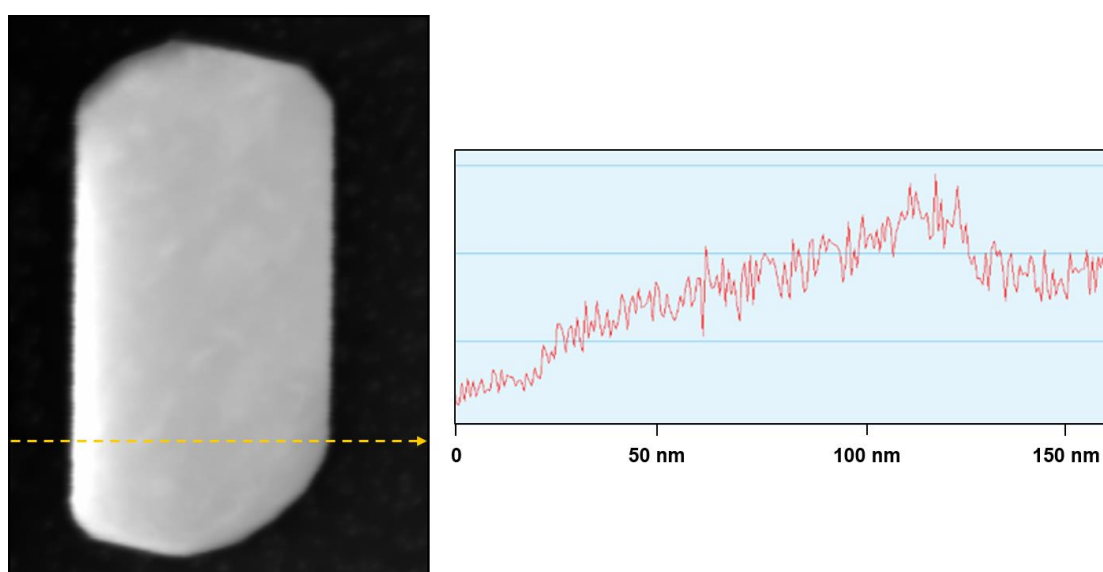


**Figure 3.14** Cross-sectional HAADF image (left) and EDX line profile taken for oxygen (right) of an oxidised platinum nanoparticle. The nanoparticle is oriented such that the left side of the image is graphite and the right side is epoxy.



**Figure 3.15** Cross-sectional HAADF image of an oxidised platinum nanoparticle (left) and EDX map for oxygen performed on the same area (right). In the EDX map, brightness indicates oxygen content, and the nanoparticle is oriented in the same way as it is in Figure 3.14.

## **Chapter 4**

# **Nanomanipulation Experiments on Platinum Nanoparticles**

### **4.1 Manipulation Experiments on Platinum Nanoparticles: Confirmation of Structural Lubricity**

After the crystalline nature and the absence of an oxide layer on platinum nanoparticles are confirmed by structural and chemical characterization steps, manipulation experiments are conducted. These experiments are performed by using FFM to laterally manipulate platinum nanoparticles on HOPG during contact mode scanning under ambient conditions. The AFM tip approaches the nanoparticle from the side, and either climbs on top of it or pushes the nanoparticle, thus manipulating it. When the normal force is high enough to initiate lateral motion, the particle will be pushed. Otherwise, the tip moves over the particle, thus “imaging” it. A schematic of the manipulation experiments can be seen in Figure 4.1. In our experiments, it was seen that lateral manipulation was routinely achieved during contact mode scanning, even at very small normal forces ( $\leq 1$  nN), thus hinting towards minimal frictional resistance to motion between the nanoparticles and the substrate.

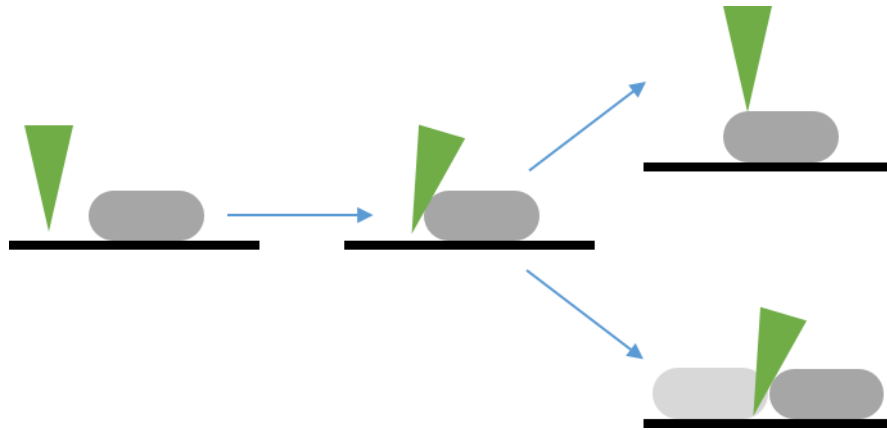


**Figure 4.1** A schematic of manipulation experiments. For small normal forces, the tip may climb on top of the particle and thus, “image” it (top). If the normal force is above a threshold value, the tip pushes the particle from the side, thus manipulating it (bottom).

For investigating the potential occurrence of structural lubricity, the friction forces experienced by the nanoparticles during manipulation as well as the size of the respective contact areas need to be determined, to probe the existence of a sub-linear relationship between them. Friction force data are gathered from lateral force images involving manipulation events, and the contact areas are determined from the topographical images of the nanoparticles. Manipulation events are associated with topography images where nanoparticles appear as though they have been “cut in half”, essentially meaning that the nanoparticle has changed its position during imaging, such that instead of the rest of the nanoparticle, the HOPG substrate is imaged after the manipulation. In the corresponding lateral force image, along the manipulation path, there would be a bright line with a higher lateral force trace than its surroundings. An example of this can be seen in Figure 4.2. Here, in the first image, a nanoparticle that has been manipulated is marked with the yellow ellipse. It can be seen there that the nanoparticle looks like it has been cut several times, hinting at the fact that the nanoparticle has been manipulated multiple times. In the second topographical image taken right after the first one, the nanoparticle appears to be stuck at an HOPG step edge, which allows the AFM tip to image the particle in its entirety, without manipulating it. The third image is the lateral force map corresponding to the manipulation events, and the lines along which the nanoparticle was manipulated can

be clearly seen as bright streaks. The voltage signal that is recorded on these streaks (minus the background signal from the HOPG substrate) directly reflects the friction force experienced by the nanoparticle during manipulation. The voltage signal is converted into force by the lateral force calibration factor  $\alpha$ , and then the mean value of the force along the manipulation path, as well as the associated minimum and maximum values, are calculated. As indicated, contact areas are measured from topography images, with a 10% error to compensate for the fact that the topography image is the convolution of the actual surface topography and the tip apex shape [49].

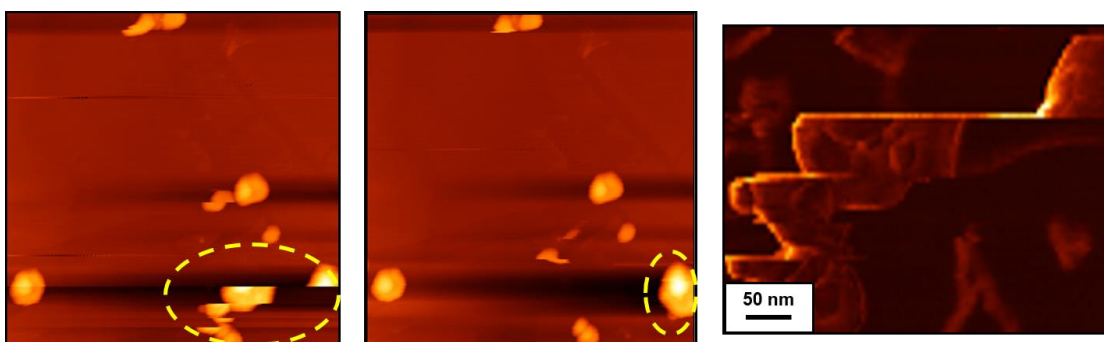


**Figure 4.2** AFM images detailing the manipulation of a platinum nanoparticle. Left: Topography image of the manipulated nanoparticle; Middle: Topography image of the nanoparticle after manipulation; Right: Lateral force image taken during manipulation.

Results of various nanomanipulation experiments performed on platinum nanoparticles are shown in Figure 4.3. Here, the friction force experienced by the nanoparticles is plotted against contact area. Also, data gathered from similar experiments performed on gold nanoparticles, which have been previously presented in Cihan *et al.* [23], are also added for comparison. The average friction force is 1.41 nN for platinum nanoparticles, and 0.33 nN for gold nanoparticles. This can be attributed to the fact that the platinum-carbon interaction is expected to be significantly stronger than the gold-carbon interaction. This can, for instance, be seen when comparing the diffusion energy barriers for gold and platinum adatoms on graphene/graphite, which have been taken as 50 meV [23] and 173 meV [50] for the calculations, respectively. Also, it can be seen in the figure that contact area sizes for gold and platinum nanoparticles are similar (hence, they are concentrated in the same region of the plot) which means rational comparisons between observed friction forces can be made for the two materials.

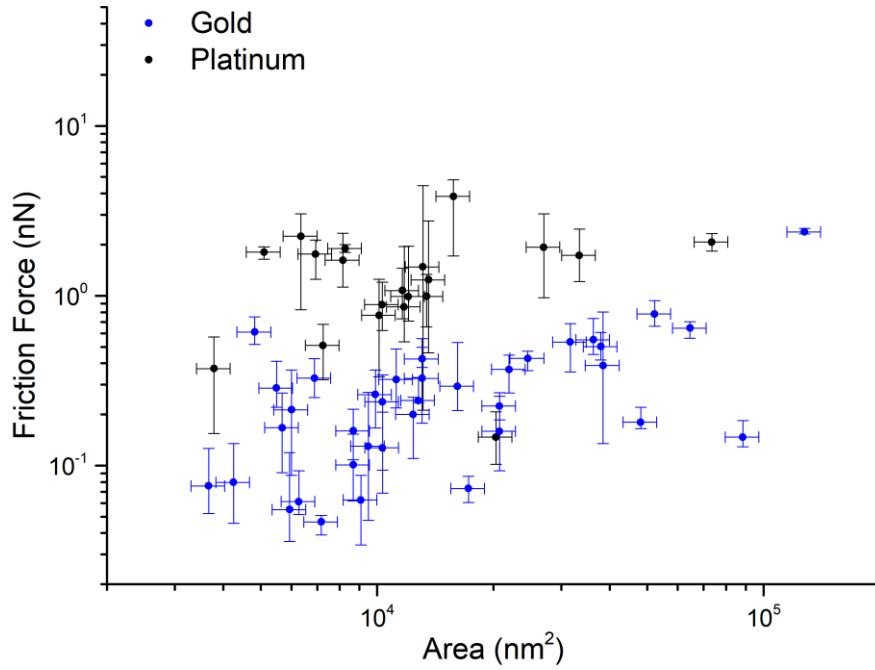


**Figure 4.3** Friction force versus contact area data points gathered from nanomanipulation experiments performed on platinum and gold nanoparticles.

To determine whether platinum nanoparticles slide on HOPG in a structurally lubric manner, the scaling factor  $\gamma$  between the number of sliding atoms and the friction force has to be calculated (see Equation 1.2). In order to do so, the friction force experienced per platinum atom,  $F_0$  has to be determined, as well. Since,

$$F_0 = \frac{\Delta E}{a} \quad (4.1)$$

where  $\Delta E$  is the diffusion energy barrier for a single platinum atom, and  $a$  is the lattice constant of the substrate; by taking  $\Delta E$  as 173 meV for platinum [50] and by taking  $a = 0.246$  nm for the graphite substrate [21] [23],  $F_0$  is found to be 0.11 nN. Friction forces are then normalized by  $F_0$ , and number of atoms on the sliding surface is calculated by multiplying the contact area with the planar density of atoms on (111) planes of platinum, which is 15.0 atoms/nm<sup>2</sup>. Results are shown in Figure 4.4. Here, the grey area limited by the blue dashed line and the red solid line denotes the range of structural lubricity, and the lines correspond to the upper and lower limits of the scaling factor  $\gamma$ , namely 0.5 and 0. As one can see from the figure, all data points are in the structural lubricity regime, with an average  $\gamma$  of 0.19. This confirms that platinum nanoparticles indeed slide in structurally lubric fashion on HOPG under

ambient conditions. Another aspect to consider here is that  $\gamma$  is expected to only depend on slider shape and orientation with respect to the substrate, and not on the specific chemical identity of the sliding atoms (since the friction force is normalized by  $F_0$ ). Comparing with gold (which has an average  $\gamma$  of 0.16 with a standard deviation of 0.06) platinum is very similar in behavior, with an average  $\gamma$  of 0.19 and a standard deviation of 0.06. This comparison shows that, as expected, as long as the slider shapes are similar (which they are), changing the material should not affect the relation between the normalized friction and the number of sliding atoms, thus confirming the validity of the theory of structural lubricity for crystalline interfaces.

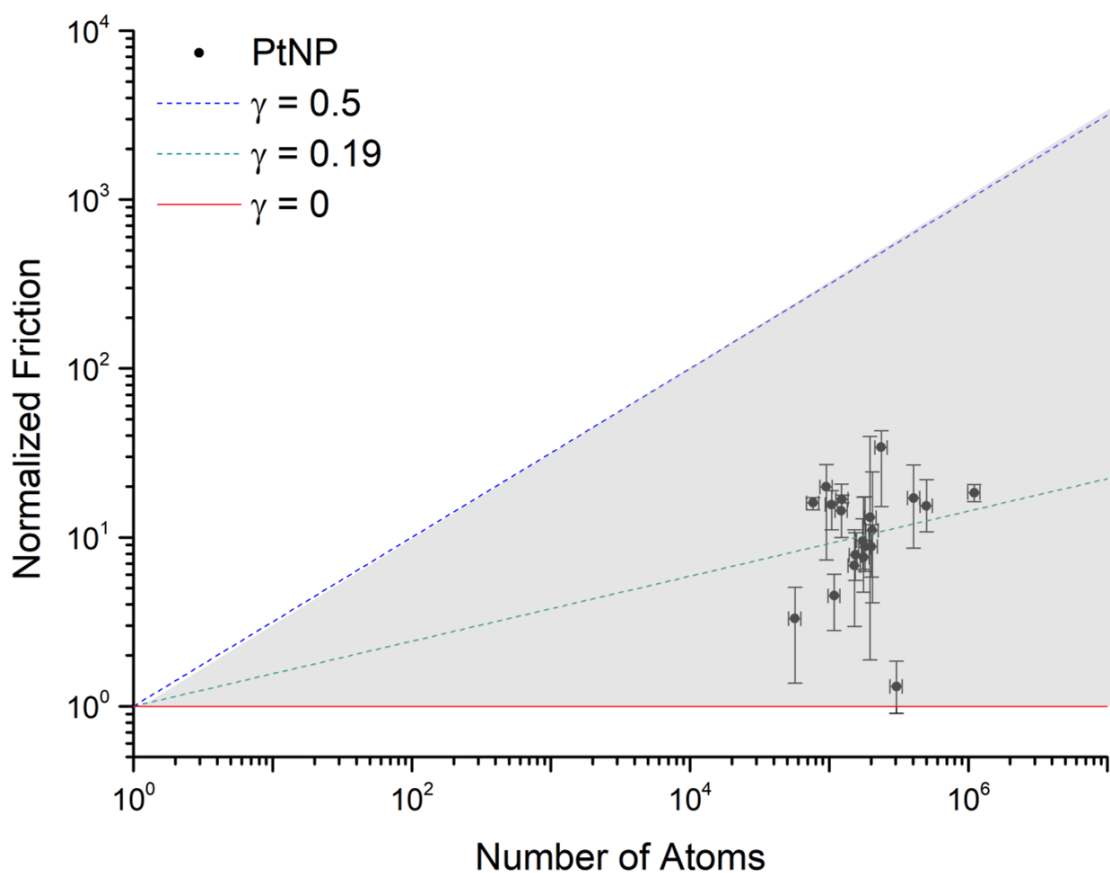


**Figure 4.4** Normalized friction versus number of sliding atoms for platinum nanoparticles. The blue dashed line and the red solid line denote the upper and lower theoretical limits of the scaling factor  $\gamma$  for structural lubricity, respectively. The cyan dashed line shows the average  $\gamma$  for all investigated nanoparticles.

## 4.2 Manipulation Experiments on Oxidised Platinum Nanoparticles

After the confirmation of structural lubricity for platinum nanoparticles sliding on HOPG under ambient conditions, the next step in this thesis involves an attempt to investigate the potential influence of interface structure and chemistry on nanoscale friction. For this investigation, platinum nanoparticles are oxidised and characterized as explained in Chapter 3. After the confirmation of oxide formation and the fact that nanoparticle morphology stays intact, nanomanipulation experiments on oxidised platinum nanoparticles have been conducted in the same manner as platinum nanoparticles. Results of these experiments, along with data points gathered from nanomanipulation experiments performed on gold and platinum nanoparticles are shown in Figure 4.5.

It can be inferred from Figure 4.5 that, on average, oxidised platinum nanoparticles experience a friction force of 11.6 nN. However, an important aspect to consider here is the fact that oxidised platinum nanoparticles are concentrated in a different region of the plot in terms of contact area; in particular, about two thirds of the investigated oxidised platinum nanoparticles are about an order of magnitude larger than most platinum and gold nanoparticles. As such, to make a sound comparison of friction forces between different nanoparticles, data points gathered from oxidised nanoparticle sliding experiments are separated into two regions (named “1” and “2”) as seen in Figure 4.5. These regions are determined by considering the contact area regime where the platinum and gold nanoparticles are concentrated. While oxidised platinum nanoparticles of large size (located in region 1) experience an average friction force of 15 nN, the nanoparticles in region 2 (which are in the same size regime as gold and platinum nanoparticles and therefore, relevant for comparison) experience an average friction force of 3.20 nN only. Therefore, it can be concluded that surface oxidation results in roughly a two-fold increase in average friction for platinum nanoparticles. Within this context, Table 4.1 summarizes mean friction forces and standard deviations for gold, platinum and oxidised platinum nanoparticles.

The observation of increased friction forces for oxidised platinum nanoparticles can be attributed to a few factors. One is that plasma oxidation could affect the HOPG substrate, and increase its roughness. This is confirmed by recording AFM topography images (with the same AFM tip) and comparing RMS roughness values of oxidised and non-oxidised samples (Figure 4.6). In the non-oxidised sample, the mean RMS roughness of HOPG is found to be 0.94 nm with a standard deviation of 0.24 nm, whereas in the oxidised sample, the mean RMS roughness is 1.53 nm with a standard deviation of 0.34 nm. This shows that there is a significant increase in the RMS roughness of HOPG after the oxidation process, which could potentially lead to the observation of increased friction forces. Another potential factor that could give rise to the observation of increased friction forces could involve the oxidation of the sliding surface of platinum nanoparticles and thus, a structural and chemical alteration of the sliding interface, as it has originally been intended. However, as explained in Chapter 3, despite the fact that XPS experiments confirmed the oxidation of platinum nanoparticles, the formation of an oxide layer on the sliding surface of the platinum nanoparticles (facing the HOPG substrate) could not be confirmed due to inconclusive cross-sectional TEM results. Combined with the fact that EDX maps also hint at a smaller concentration of oxygen on the sliding surface when compared with the top surface of nanoparticles, the potential formation of platinum oxide on the sliding surface cannot be confirmed at this point; and as such, an association with the observation of increased friction forces cannot be formed.

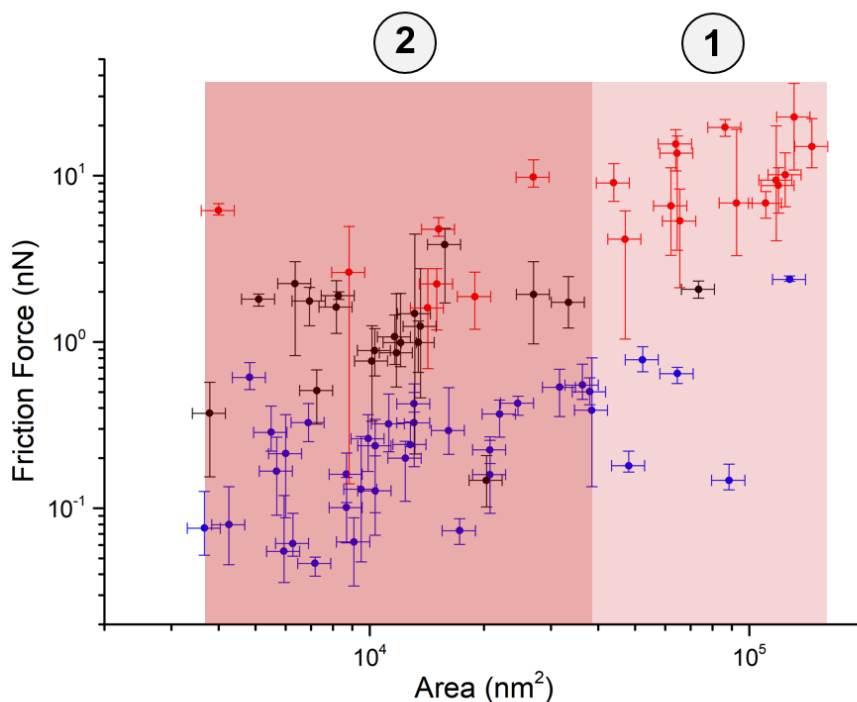


**Figure 4.5** Friction force versus contact area data points gathered from oxidised platinum nanoparticles sliding on graphite (red), compared with gold (blue) and platinum (black) data points. The plot has been divided into two size regimes, where regime 2 includes data points relevant for a comparison of friction forces between the different types of materials.

**Table 4.1** Mean friction forces and standard deviations for gold, platinum and oxidised platinum nanoparticles with similar contact areas

NP Type ( <i>similar areas</i> )	Mean (nN)	Standard Deviation (nN)
Au-NP	0.33	0.39
Pt-NP	1.41	0.83
Pt-Oxide-NP	3.20	1.83

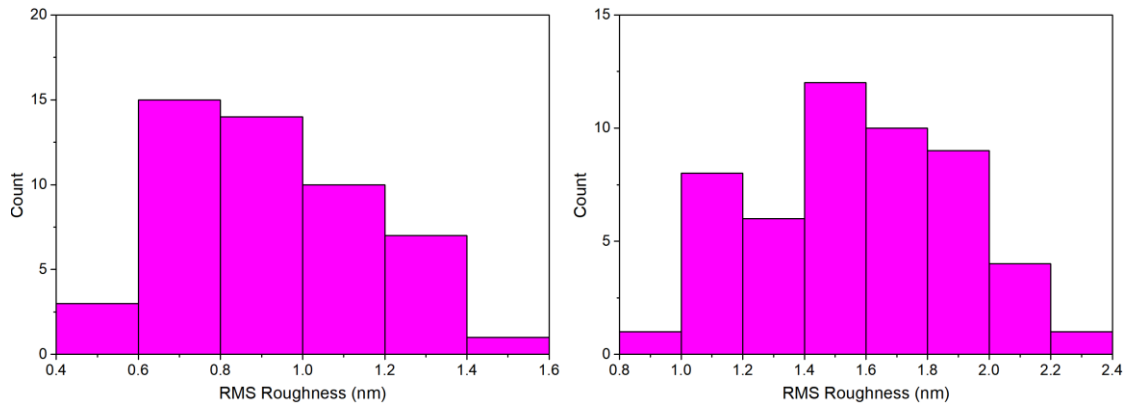


**Figure 4.6** RMS roughness histograms of HOPG in non-oxidised (left) and oxidised (right) samples.

## Chapter 5

### Summary and Outlook

This thesis has focused on the question of whether structural lubricity under ambient conditions is exclusive to gold nanoparticles sliding on graphite [23] or whether it could be extended to other noble metals, too. To answer this question, nanomanipulation experiments have been performed under ambient conditions on platinum nanoparticles situated on graphite via AFM. Sample preparation has been achieved via e-beam evaporation of minimal amounts of platinum on graphite, followed by post-deposition annealing. Nanoparticles have been thoroughly characterized by SEM, TEM and XPS; and the results confirmed that platinum nanoparticles exhibit clean, crystalline and atomically flat surfaces under ambient conditions. Subsequently, nanomanipulation experiments have been conducted on the nanoparticles using a commercial AFM setup under typical laboratory conditions. Results of these experiments showed that platinum nanoparticles indeed slide in structurally lubric fashion under ambient conditions, with an average scaling factor  $\gamma$  of 0.19. Additionally, it is seen that platinum nanoparticles on average experience approximately four times more friction during sliding on graphite when compared with gold nanoparticles, which can be attributed to stronger interaction between platinum and carbon atoms when compared with the interaction of gold and carbon atoms. On the other hand,  $\gamma$  values of gold ( $0.16 \pm 0.06$ ) and platinum ( $0.19 \pm 0.06$ ) are

remarkably close to each other. This result is in good agreement with the theory of structural lubricity for crystalline interfaces, which states that the scaling factor is expected to be invariant of material type, but only depends on slider shape and orientation with respect to the substrate.

After the confirmation of structural lubricity on platinum nanoparticles under ambient conditions, an attempt has been made in the last part of the thesis to oxidise the sliding platinum surface and thus study the effects of altering the interface structure and chemistry on friction. For this purpose, platinum nanoparticles have been oxidised by reactive oxygen plasma. While characterization via SEM showed no significant change in morphology, XPS results firmly confirmed the existence of platinum oxide. Nanomanipulation experiments conducted on oxidised nanoparticles showed that, in the same size range, oxidised platinum nanoparticles experience approximately two times more friction than platinum nanoparticles. However, a straightforward connection between the observation of increased friction forces and oxidation of the sliding surface could not be formed due to, (i) the increased roughness of the graphite substrate upon plasma treatment (which could also contribute to the increase in friction) and (ii) inconclusive cross-sectional TEM experiments with which the existence of an oxide layer at the sliding interface could not be observed. As such, the detailed investigation of the relationship between surface oxidation and friction on the nanoscale remains a subject for future work.

# Bibliography

- [1] G. Cadoret and A. M. Smith, “Friction, not texture, dictates grip forces used during object manipulation,” *J. Neurophysiol.*, vol. 75, no. 5, pp. 1963–1969, 1996.
- [2] H.-Y. Han, A. Shimada, and S. Kawamura, “Analysis of friction on human fingers and design of artificial fingers,” in *Proceedings of the 1996 International Conference on Robotics and Automation*, pp. 3061–3066, 1996.
- [3] C. M. Mate, “Force Microscopy Studies of the Molecular Origins of Friction and Lubrication,” *IBM J. Res. Dev.*, vol. 39, no. 6, pp. 617–627, 1995.
- [4] K. Holmberg, P. Andersson, and A. Erdemir, “Global energy consumption due to friction in passenger cars,” *Tribol. Int.*, vol. 47, pp. 221–234, 2012.
- [5] K. Holmberg, R. Siilasto, T. Laitinen, P. Andersson, and A. Jäsberg, “Global energy consumption due to friction in paper machines,” *Tribol. Int.*, vol. 62, pp. 58–77, 2013.
- [6] K. Holmberg, P. Andersson, N. O. Nylund, K. Mäkelä, and A. Erdemir, “Global energy consumption due to friction in trucks and buses,” *Tribol. Int.*, vol. 78, pp. 94–114, 2014.
- [7] F. Berna *et al.*, “Microstratigraphic evidence of in situ fire in the Acheulean strata of Wonderwerk Cave, Northern Cape province, South Africa,” *Proc. Natl. Acad. Sci.*, vol. 109, no. 20, pp. E1215–E1220, 2012.
- [8] M. Nosonovsky, “Oil as a Lubricant in the Ancient Middle East,” *Tribol. Online*, vol. 2, no. 2, pp. 44–49, 2007.
- [9] I. M. Hutchings, “Leonardo da Vinci’s studies of friction,” *Wear*, vol. 360–361, pp. 51–66, 2016.
- [10] G. Amontons, “De la resistance causée dans les Machines, tant par les frottemens des parties qui les composent, que par roideur des cordes qu’on y employe, & la maniere de calculer l’un & l’autre,” *Hist. l’Académie R. des Sci.*,

pp. 206–222, 1699.

- [11] M. Urbakh, J. Klafter, D. Gourdon, and J. Israelachvili, “The nonlinear nature of friction,” *Nature*, vol. 430, pp. 525–528, 2004.
- [12] F. P. Bowden and D. Tabor, *The Friction and Lubrication of Solids*. Oxford: Oxford University Press, 2001.
- [13] I. Szlufarska, M. Chandross, and R. W. Carpick, “Recent advances in single-asperity nanotribology,” *J. Phys. D. Appl. Phys.*, vol. 41, no. 12, p. 123001, 2008.
- [14] B. Bhushan, J. N. Israelachvili, and U. Landman, “Nanotribology: friction, wear and lubrication at the atomic scale,” *Nature*, vol. 374, no. 6523, pp. 607–616, 1995.
- [15] J. N. Israelachvili *et al.*, “Recent advances in the surface forces apparatus (SFA) technique,” *Reports Prog. Phys.*, vol. 73, p. 036601, 2010.
- [16] G. Binnig, H. Rohrer, C. Gerber, and E. Weibel, “Surface studies by scanning tunneling microscopy,” *Phys. Rev. Lett.*, vol. 49, no. 1, pp. 57–61, 1982.
- [17] G. Binnig and C. F. Quate, “Atomic Force Microscope,” *Phys. Rev. Lett.*, vol. 56, no. 9, pp. 930–933, 1986.
- [18] H. Hölscher, U. Schwarz, O. Zwörner, and R. Wiesendanger, “Consequences of the stick-slip movement for the scanning force microscopy imaging of graphite,” *Phys. Rev. B*, vol. 57, no. 4, pp. 2477–2481, 1998.
- [19] M. Dienwiebel, G. S. Verhoeven, N. Pradeep, J. W. M. Frenken, J. A. Heimberg, and H. W. Zandbergen, “Superlubricity of graphite,” *Phys. Rev. Lett.*, vol. 92, no. 12, p. 126101, 2004.
- [20] M. M. Van Wijk, M. Dienwiebel, J. W. M. Frenken, and A. Fasolino, “Superlubric to stick-slip sliding of incommensurate graphene flakes on graphite,” *Phys. Rev. B*, vol. 88, no. 23, p. 235423, 2013.
- [21] D. Dietzel, M. Feldmann, U. D. Schwarz, H. Fuchs, and A. Schirmeisen, “Scaling laws of structural lubricity,” *Phys. Rev. Lett.*, vol. 111, no. 23, p.

235502, 2013.

- [22] D. Dietzel *et al.*, “Interfacial friction obtained by lateral manipulation of nanoparticles using atomic force microscopy techniques,” *J. Appl. Phys.*, vol. 102, no. 8, p. 084306, 2007.
- [23] E. Cihan, S. Ipek, E. Durgun, and M. Z. Baykara, “Structural lubricity under ambient conditions,” *Nat. Commun.*, vol. 7, p. 12055, 2016.
- [24] M. H. Müser, “Structural lubricity: Role of dimension and symmetry,” *Europhys. Lett.*, vol. 66, no. 1, pp. 97–103, 2004.
- [25] M. Hirano and K. Shinjo, “Atomistic locking and friction,” *Phys. Rev. B*, vol. 41, no. 17, pp. 11837–11851, 1990.
- [26] A. Erdemir and J.-M. Martin, *Superlubricity*. Amsterdam: Elsevier, 2007.
- [27] E. Meyer and E. Gnecco, “Superlubricity on the nanometer scale,” *Friction*, vol. 2, no. 2, pp. 106–113, 2014.
- [28] A. E. Filippov, M. Dienwiebel, J. W. M. Frenken, J. Klafter, and M. Urbakh, “Torque and twist against superlubricity,” *Phys. Rev. Lett.*, vol. 100, no. 4, p. 046102, 2008.
- [29] A. S. De Wijn, “(In)commensurability, scaling, and multiplicity of friction in nanocrystals and application to gold nanocrystals on graphite,” *Phys. Rev. B*, vol. 86, no. 8, p. 085429, 2012.
- [30] H. Hölscher, A. Schirmeisen, and U. D. Schwarz, “Principles of atomic friction: from sticking atoms to superlubric sliding,” *Philos. Trans. R. Soc. A*, vol. 366, no. 1869, pp. 1383–1404, 2008.
- [31] G. He, M. H. Müser, and M. O. Robbins, “Adsorbed Layers and the Origin of Static Friction,” *Science*, vol. 284, no. 5420, pp. 1650–1652, 1999.
- [32] M. Knoll and E. Ruska, “Das Elektronenmikroskop,” *Zeitschrift für Phys.*, vol. 79, no. 9–10, pp. 318–339, 1932.
- [33] “The Nobel Prize in Physics 1986,” *Nobel Media AB 2014*, 2017. [Online]. Available: [http://www.nobelprize.org/nobel\\_prizes/physics/laureates/1986/](http://www.nobelprize.org/nobel_prizes/physics/laureates/1986/).

- [34] M. von Ardenne, “Das Elektronen-Rastermikroskop - Theoretische Grundlagen,” *Zeitschrift für Phys.*, vol. 108, no. 338, pp. 553–572, 1938.
- [35] J. Goldstein *et al.*, *Scanning Electron Microscopy and X-ray Microanalysis*, 3rd ed. New York: Kluwer Academic/Plenum Publishers, 2003.
- [36] A. Dâna, MSN 510 Lecture Notes: “Imaging Techniques in Materials Science and Nanotechnology”, UNAM, Bilkent University, Ankara, 2015.
- [37] M. Z. Baykara, T. C. Schwendemann, E. I. Altman, and U. D. Schwarz, “Three-Dimensional Atomic Force Microscopy – Taking Surface Imaging to the Next Level,” *Adv. Mater.*, vol. 22, pp. 2838–2853, 2010.
- [38] P. Eaton and P. West, *Atomic Force Microscopy*. Oxford: Oxford University Press, 2010.
- [39] G. Meyer and N. M. Amer, “Simultaneous measurement of lateral and normal forces with an optical-beam-deflection atomic force microscope,” *Appl. Phys. Lett.*, vol. 57, no. 20, pp. 2089–2091, 1990.
- [40] S. Sundararajan and B. Bhushan, “Topography-induced contributions to friction forces measured using an atomic force/friction force microscope,” *J. Appl. Phys.*, vol. 88, no. 8, p. 4825, 2000.
- [41] J. E. Sader, I. Larson, P. Mulvaney, and L. R. White, “Method for the calibration of atomic force microscope cantilevers,” *Rev. Sci. Instrum.*, vol. 66, no. 7, pp. 3789–3798, 1995.
- [42] M. L. B. Palacio and B. Bhushan, “Normal and Lateral Force Calibration Techniques for AFM Cantilevers,” *Crit. Rev. Solid State Mater. Sci.*, vol. 35, no. 2, pp. 73–104, 2010.
- [43] M. Varenberg, I. Etsion, and G. Halperin, “An improved wedge calibration method for lateral force in atomic force microscopy,” *Rev. Sci. Instrum.*, vol. 74, no. 7, pp. 3362–3367, 2003.
- [44] E. Cihan, A. Özoğul, and M. Z. Baykara, “Structure and nanotribology of thermally deposited gold nanoparticles on graphite,” *Appl. Surf. Sci.*, vol. 354,

pp. 429–436, 2015.

- [45] Z. Li, P. Beck, D. A. A. Ohlberg, D. R. Stewart, and R. S. Williams, “Surface properties of platinum thin films as a function of plasma treatment conditions,” *Surf. Sci.*, vol. 529, no. 3, pp. 410–418, 2003.
- [46] S. S. Datta, D. R. Strachan, S. M. Khamis, and A. T. C. Johnson, “Crystallographic etching of few-layer graphene,” *Nano Lett.*, vol. 8, no. 7, pp. 1912–1915, 2008.
- [47] C. D. Wagner *et al.*, *Handbook of X-Ray Photoelectron Spectroscopy*, vol. 3, no. 4. Minnesota: Perkin-Elmer Corporation, 1979.
- [48] K. S. Kim, N. Winograd, and R. E. Davis, “Electron spectroscopy of platinum-oxygen surfaces and application to electrochemical studies,” *J. Am. Chem. Soc.*, vol. 93, no. 23, pp. 6296–6297, 1971.
- [49] C. Ritter, M. Heyde, B. Stegemann, K. Rademann, and U. D. Schwarz, “Contact-area dependence of frictional forces: Moving adsorbed antimony nanoparticles,” *Phys. Rev. B*, vol. 71, no. 8, p. 085405, 2005.
- [50] X. Liu *et al.*, “Metals on graphene: correlation between adatom adsorption behavior and growth morphology,” *Phys. Chem. Chem. Phys.*, vol. 14, no. 25, p. 9157, 2012.